Mesoscale variability of the Antarctic Slope Front and the Slope Current

Master's thesis in,
Physical Oceanography

Andriani Glykofridi-Fragkou

GEOPHYSICAL INSTITUTE

01 June 2022

Acknowledgements

Firstly, I would like to thank Kjersti Daae for allowing me to work on exciting moorings in the Southeastern Weddell Sea. Her help and support in dealing with and understanding the challenges in the water masses and atmospheric data were undeniably valuable. She always offered feedback and motivated me to search the Antarctic Slope Front in detail.

My second thanks go to Vår Dundas for helping me understand the variability in hydrography, providing me feedback when I needed. Our discussion helped me to understand the importance of studying the Weddell Sea.

Finally, I would like to thank my family and friends for supporting me during my master and motivating me to continue the hard work. Without them, I would not be able to chase my dreams and challenge myself.

Abstract

The Weddell Sea is essential for the global climate due to the production of the dense shelf water that contributes to the Weddell Sea Bottom Water (WSBW), feeding the lower limb of the global thermohaline circulation (Orsi et al., 1999). The Weddell Sea continental shelf region is currently protected from the inflow of warm water by the Antarctic Slope Front (ASF). However, we do not know how the slope front will change with the ongoing global warming, and we are concerned about the climatic response if warm water gains access to the continental shelf and accelerate the ice shelf melt rates. We study which mechanisms influence the mesoscale variability of the ASF and the associated Antarctic Slope Current (ASC). We base our study on two mooring arrays located at the eastern flank of the Filchner Trough opening and one mooring array 450 km upstream at 17° W, atmospheric data from the ERA5 reanalysis dataset, and sea ice motion from the NSIDC dataset. We set up time series analysis, frequency spectra and lagged correlations with 15 days of low pass filtering techniques. We find that the thermocline lies at depths of 400-1000 m. The lag in mesoscale variability between the along flow current at the two mooring arrays is shorter than the advective time scale. Combined with high correlation with atmospheric parameters, we conclude that the surface stress and Ekman pumping are strongly influencing the mesoscale variability of the Antarctic slope current. The lag correlation between absolute salinity in the two areas indicates that the variability we see in salinity could be a mix of direct atmospheric forcing and advection.

Acronyms

- ACC: Antarctic Circumpolar Current
- ASF: Antarctic Slope Front
- ASC: Antarctic Slope Current
- ASW: Antarctic Surface Water
- CDW: Circumpolar Deep Water
- ESW: Eastern Shelf Water
- FT: Filchner Trough
- FIS: Filchner Ice Shelf
- FRIS: Filchner-Rone Ice Shelf
- HSSW: High Salinity Shelf Water
- ISW: Ice Shelf Water
- RIS: Ronne Ice Shelf
- MCDW: Modified Circumpolar Deep Water
- MWDW: Modified Warm Deep Water
- SIC: Sea Ice Concentration
- SLP: Sea Level Pressure
- WDW: Warm Deep Water
- WSBW: Weddell Sea Bottom Water
- WSDW: Weddell Sea Deep Water
- WW: Winter Water
- mslp: mean sea level pressure

Contents

Chapter 1

Introduction

Antarctica is a remote area surrounded by the ocean and covered with snow and ice. While Antarctica is far from Greece, where I come from, changes in Antarctica can impact the entire planet. Therefore, awareness of this region's atmospheric and oceanic processes is important to increase our understanding of Antarctica's connection to the global climate system. Two main mechanisms make Antarctica important for our planet.

Firstly, Antarctica produces dense bottom water, formed at several locations along the Antarctic continental shelf and constitutes the lower limb of the global thermohaline circulation (Orsi et al., 1999). Secondly, the melting of ice shelves enhances the flow of grounded ice into the ocean. That leads to global sea-level rise, and the meltwater input can affect the formation of dense bottom water (Heywood et al., 1985).

The Weddell Sea Bottom Water (WSBW), ultimately transformed into the Antarctic Bottom Water (AABW), is an important water mass for global climates. It is a part of the global circulation and fills the deepest regions of the world oceans. The Weddell Sea ice shelves play major roles in the production of WSBW; High Salinity Shelf Water (HSSW) is produced near Filchner-Ronne Ice Shelf (FRIS) due to cooling from the atmosphere in winter (Foldvik et al., 2004; Foldvik and Gammelsrød, 1988; Mueller and Timmermann, 2019). The HSSW enters the FRIS cavity. Since the HSSW has a temperature near the surface freezing point, it can drive melting deep in the ice shelf cavity, where the pressure decreases the melting point below the surface freezing point. The HSSW mixes with the ice shelf meltwater and is transformed into Ice Shelf Water (ISW). The ISW can fill the Filchner Trough and spill over the sill. When the ISW descends the continental slope, it mixes with ambient water to form WSBW, guiding thermohaline circulation in the global abyssal ocean (Morrison et al., 2020).

The conditions in which ice shelves change are the key to understanding the ice-ocean interaction and how they can contribute to sea-level rise. Modelling studies have already shown that the continuous changes in the exchange between ice shelves and the ocean due to changes in atmospheric conditions might support the southward heat transport in the Filchner Ice Shelf cavity through the Filchner Trough (Hellmer H., 2012; Timmermann and Hellmer, 2013). While few ice shelves along the Antarctic Peninsula have collapsed since the 1940s (Mueller and Timmermann, 2019), the melt rate of

ice shelves in the Southern Weddell Sea is currently low (Rignot and Mouginot, 2013). However, due to global warming, the future of the ice shelves is uncertain, and their response is still unclear.

In addition, the fate of the Filchner-Ronne Ice Shelf (FRIS) depends on the ocean processes along the continental slope upstream of the Filchner Trough. The interaction between the water masses adjacent to the continental shelf break can explain essential processes preventing or allowing warm water to flow into the Filchner Trough and towards the ice shelf cavities. If the warm water from the open ocean gets access to the Filchner Ice Shelf (FIS) cavity, it may increase the melt rate of the ice shelf. Consequently, the heat transport into the Ice shelf can affect the stability of the Antarctic Ice Sheet (Daae, 2018). While the FRIS is a cold regime ice shelf today (Thompson et al., 2018), the intrusion of warm water might lead the FRIS into a warm regime (Hellmer H., 2012). Although modelling studies have shown that this is possible, this is not realistic due to dense water in the FT (Daae et al., 2020).

An oceanic front near the Antarctic, described as Antarctic Slope Front (ASF), strongly controls the melting of ice shelves. It prevents the relatively warm water in the deep ocean from flowing onto the continental shelf. It can potentially reach the ice shelf cavities and contribute to the melting of ice shelves from below. Here, we study the mesoscale variability of the atmospheric forcing and water masses along the continental slope of the Southeastern Weddell Sea. We will learn more about the mechanisms that affect the ASF and, therefore also, the shelf-ocean water exchange.

The ASF is an oceanic feature near the shelf break, which is distinguished by strong subsurface gradients in ocean temperature (Jacobs, 1991). The ASF separates the cold and fresh surface water on the continental shelf from the warmer and saltier WDW in the open ocean (Daae, 2018; Gill, 1973; Jacobs, 1991). Easterly winds along the coast lead to onshore Ekman transport (Daae, 2018; Deacon, 1937; Sverdrup, 1954) and induce the downward sloping isotherms of the ASF. The main mechanisms across the continental slope have already been studied. We aim to describe how these mechanisms drive the mesoscale variability in ASF in observations. When the easterly wind is weak, the ASF relaxes. Although we see that warm water reaches the ice shelf cavity at the Bellinghausen Sea (Thompson et al., 2018), where the isopycnals relax, the relaxation of the ASF is not necessarily sufficient to bring warm water into the ice shelf cavity. The southward transport of warm water also depends on the conditions inside the Filchner Trough. The presence of dense shelf water (HSSW/ISW) in the trough can block the inflow of warm water (Daae et al., 2020), and favourable conditions for warm inflow do not occur regularly (Darelius et al., 2016). However, the knowledge of ASF variability will help us understand whether the warm water is available at depths where it can access the continental shelves or not.

Five moorings from the University of Bergen (the M-moorings) were deployed between February 2009 and February 2010 on the slope of the Crary Fan east of the leading outflow site of the Flchner overflow plume (Jensen et al., 2013) (fig: 1.1). During the same period, five moorings from the SASSI project (Synoptic Antarctic Shelf Slope Interactions) were deployed further east at $\sim$17° W (Graham et al., 2013).

Many moorings have been deployed in the Weddell Sea, but they have been used to

analyze different processes. The M and the SASSI moorings datasets are from the same year, but they have not been studied together before. Combining mooring observations from other areas in the Weddell Sea gives new opportunities to study the mesoscale variability over the continental slope. We focus on the processes that drive the mesoscale variability of the ASF and ASC. We study the local atmospheric forcing in the M- and the SASSI areas to find a link between the atmospheric forcing with hydrographic and currents variability at each mooring area.

In section 2, we present the study area and briefly describe the Weddell Sea and its main circulation. Section 3 describes the datasets and methods to obtain our results. In section 4, we present the characteristics of the water masses as seen from mooring observations. We also present the variability in surface stress and the Ekman pumping anomaly in M and SASSI areas. In section 5, we discuss the main results of our analysis. In section 6, we discuss our conclusions.

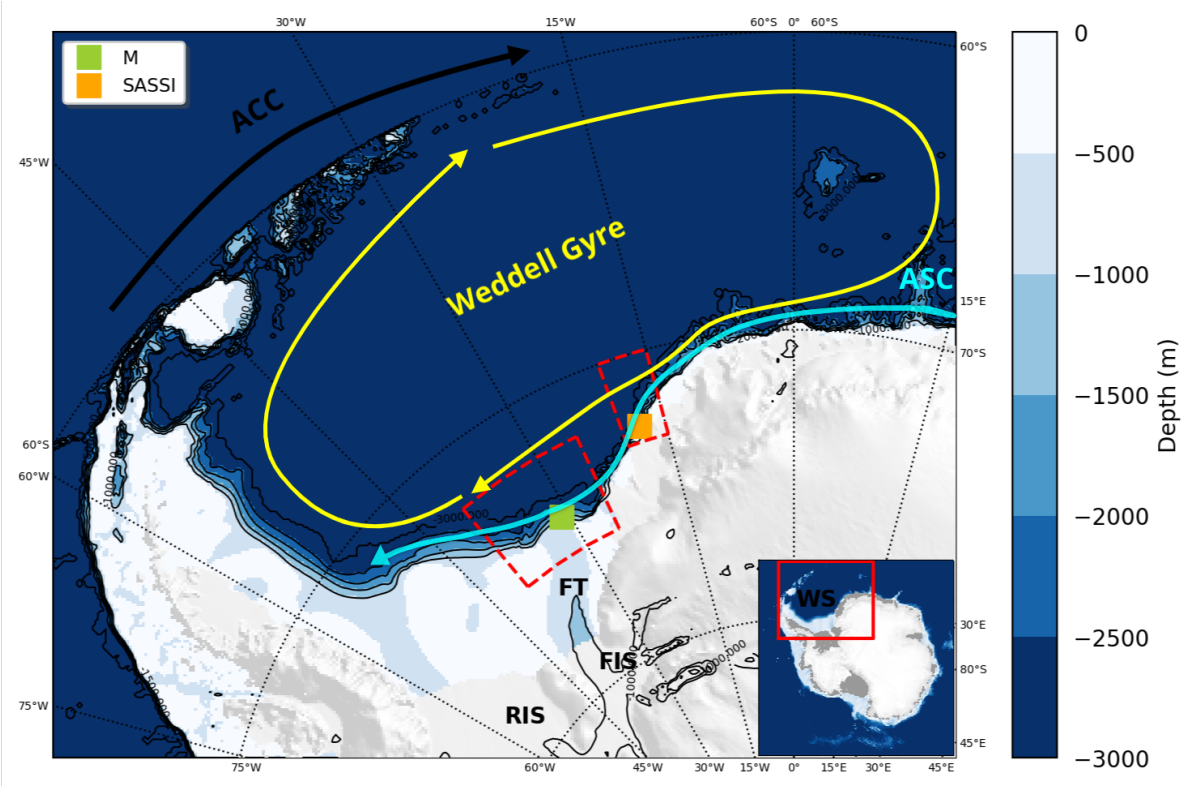

Figure 1.1: Map of the study region showing the position of the M-moorings (green) ∼ 30° W and SASSI-moorings (orange) ∼ 17° W in the Weddell Sea. Black lines are isobath (Fretwell et al., 2013b) between 1000 and 3000 m depths. We show the land and the floating ice shelf in light grey. The inset shows an overview of Antarctica and the Weddell Sea (WS) location in a red box. Here, we present the land, floating ice shelves in light grey and the floating ice shelves in dark grey. The big figure shows the Ronne Ice shelf (RIS), the Filchner Ice shelf (FIS), and the Filchner Trough (FT). The red dashed squares indicate the area of M-moorings and Sassi-moorings, where we extract the atmospheric forcing from ERA5 data. The west square has latitude [75.5°S, 72°S] and longitude [40°W, 20°W] and the east one with latitude [73°S, 70°S] and longitude [20°W, 15°W]. We give an overview of the Antarctic circumpolar current (ACC) (black), Weddell Gyre (WG) (yellow), and the Antarctic Slope Current (ASC) (cyan) directions (Mueller and Timmermann, 2019; Thompson et al., 2018; Daae, 2018; Darelius et al., 2016; Nicholls et al., 2009). The Bedmap2 do not provide bathymetry data north of 60° S (Fretwell et al., 2013b).

Chapter 2

Background

2.1 Overview of the Weddell Sea

2.1.1 Ice shelves and the main circulation

We study the continental shelf break and continental slope front regions in the south-eastern Weddell Sea, Antarctica. The bathymetry shows the Antarctic continental shelf and the Antarctic continental slope, the ice shelves, and the ocean (fig: 1.1). The Filchner-Rone Ice Shelf (FRIS) combines the Filchner ice shelf (FIS) in the east and the Ronne ice shelf (RIS) in the west. The FRIS floats over the southern part of the Weddell Sea continental shelf. It has a 450,000 km^2 volume of ice, (Nicholls et al., 2009) and its thickness ranges from 100 m to the deep grounding line at 1500 m (Mueller and Timmermann, 2019; Nicholls et al., 2009). On the eastern side of the FRIS, icebergs can release and follow the path of the ocean current. The Filchner Trough (FT) starts in the ice shelf cavity under the FIS and goes cross to the continental shelf break. The dense Ice shelf Water (ISW) that comes out from the FRIS cavity, fills up the FT and overflows the FT sill (600 m) (Darelius et al., 2014).

All around Antarctica (fig: 1.1), the Antarctic circumpolar current (ACC) flows eastward and is driven from westerly winds (Hogg, 2010). The lack of any landmass connecting with Antarctica explains the circumpolar feature of the ACC. In addition, a combination of ridges, continental shelves, and the Antarctic Peninsula also guides the ACC (Mueller and Timmermann, 2019). Katabatic winds over ice sheets and glaciers turn towards west due to the corriolis effect (Mueller and Timmermann, 2019). The combination of easterlies in the south and westerlies in the north generates the Antarctic divergence (Deacon, 1979) and drives the cyclonic circulation of the Weddell Gyre (WG) (Vernet et al., 2019).

The Weddell Gyre (WG) is an oceanographic feature of the Southern Ocean south of the ACC that covers $5.6x10^2$ km^2 and make the heat more easily available far south (Mueller and Timmermann, 2019) bringing the warm water from the east in Weddell Sea. The WG extends from south of 55-60^oS and between 60^oW and 30^oE roughly (Vernet et al., 2019; Deacon, 1979). The Antarctic continent and the Antarctic Peninsula constrain south and west of the gyre, and the southern ACC forms the northern

boundary. The eastern side of the WG does not meet any lands and does not fix. Here, the gyre can extend as far east at 70^oE (Vernet et al., 2019). The Antarctic divergence could lead to relatively warm subsurface waters and high sea-ice formation. Air-sea exchanges and heat flow, therefore, make the WG meaningful for the exhanges of water masses in the Weddell Sea (Vernet et al., 2019). The combination of upwelling and downwelling that plays a role in the global overturning circulation introduces complex processes of the water masses. Due to sea-ice cover, studying the WG is still challenging.

2.1.2 Water masses in the Southern Weddell Sea

Around Antarctica, we find the CDW (fig: 1.1), a relatively warm, salty, and nutrient-rich water mass (Dinniman et al., 2012). The CDW is a component of the ACC warmer above the freezing point. The CDW enters the Weddell Sea from the northeast of the Weddell Gyre, and due to cooling and freshening along this pathway, it is redefined as Warm Deep Water (WDW) (fig: 2.1) (Nicholls et al., 2009; Mueller and Timmermann, 2019). The onshore transport of the WDW towards the continental shelf is limited by the presence of the Antarctic Slope Front (ASF) (Heywood et al., 1985). At specific locations in Antarctica, the WDW can flow on the continental shelf. When it reaches as far south as the ice shelf cavities, it can lead to melt (Thompson et al., 2018). The melt rate depends on the changes in the frequency and extent of cross-shelf intrusion of WDW (Dinniman et al., 2012).

Above the WDW, we find the Antarctic Surface water (ASW). In winter, the ASW cools to the freezing point due to heat loss in the atmosphere. Due to ice production, the ASW is transformed into Winter Water (WW), which is cold and salty water, has practical salinity between 34.36 and 34.52 (fig: 2.1, 2.2) (Foldvik et al., 1985). The mixing between WW and WDW below creates the intermediate Modified Warm Deep Water (MWDW) (fig: 2.2) (Foster and Carmack, 1976; Nicholls et al., 2009; Foldvik et al., 1985; Mueller and Timmermann, 2019).

Further cooling of MWDW and brine rejection from sea ice formation on the continental shelf form High Salinity Shelf Water (HSSW) at a near-surface freezing point (Nicholls et al., 2009; Darelius et al., 2014). Since increasing pressure reduces the freezing point of saltwater, the HSSW is supercooled at great depths. The HSSW enters the FRIS cavity from the western flank of the Berkner island (Nicholls et al., 2009) and circulates along with the southern flank of the island (Nicholls et al., 2009). Through the interaction with the ice cavity, the HSSW can drive basal melting (Lewis and Perkin, 1986; Nicholls et al., 2009) and be transformed into Ice Shelf Water (ISW) (Darelius et al., 2014). HSSW can also descend the continental slope and interact with WDW and MWDW (Gill, 1973).

The Ice Shelf Water (ISW) is a dense and cold water mass with a temperature below the surface freezing point at the base of the Antarctic ice shelves (Nicholls et al., 2009) (fig: 2.1). It can flow northward out of the ice shelf cavity through the FT (Daae et al., 2018) and spill over the trough at 1,6 Sv (Darelius et al., 2014). Darelius et al. (2014) frequently notice the ISW in a 150 m thick layer at the sill. When the ISW descends the slope of the Filchner Trough, it forms a dense overflow plume and is referred to as Filchner overflow. This gravity plume is affected by the rotation of the Earth. When it crosses the FT sill, it moves west of the Berkner island and flows westward along the continental slope (Foldvik et al., 1985; Nicholls et al., 2009). Thus, it contributes to the formation of AABW (Foldvik et al., 2004; Darelius et al., 2014; Daae et al., 2020), which leads to the thermohaline circulation in the global abyssal ocean (Morrison et al., 2020). The HSSW and ISW are essential for forming Weddell Sea Deep Water (WSDW) and Weddell Sea Bottom Water (WSBW).

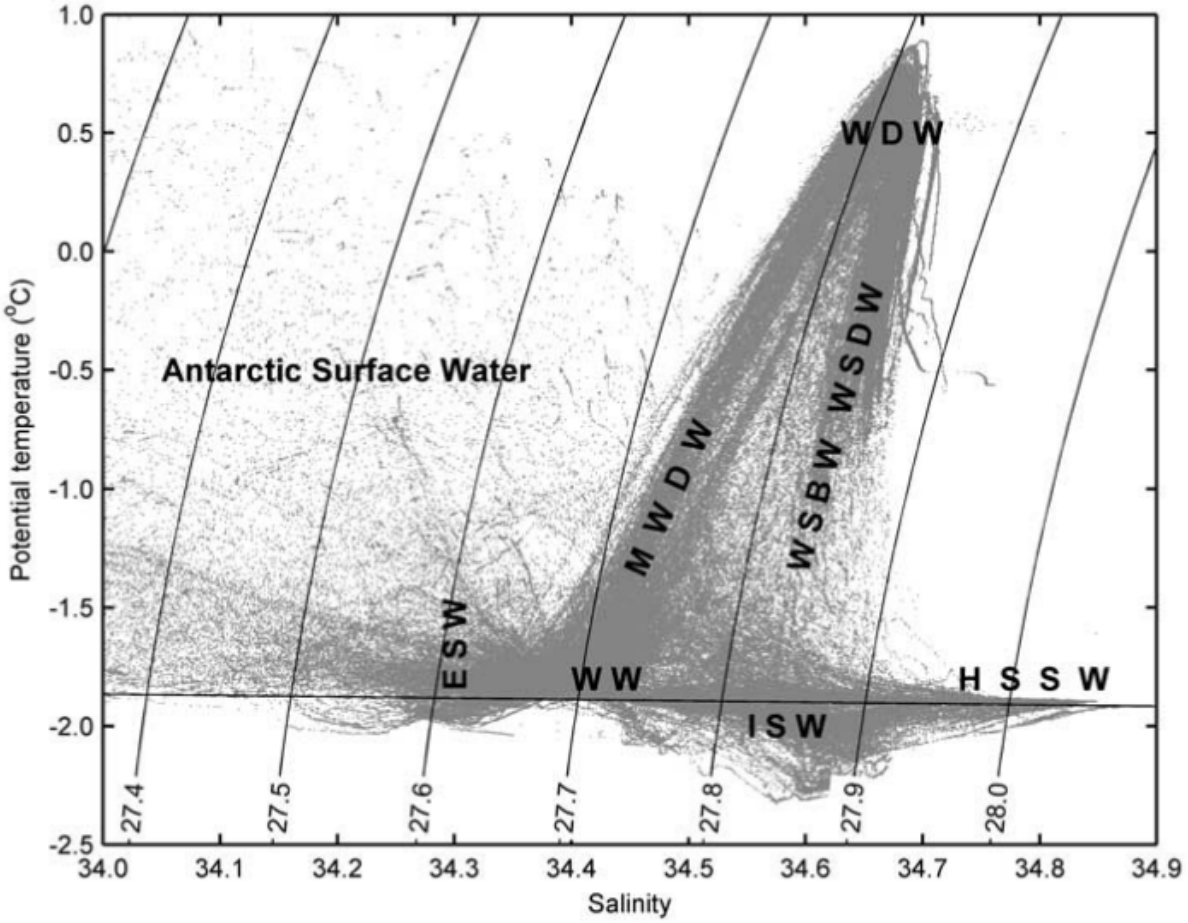

Figure 2.1: A $\Theta - S_A$ diagram showing data from 554 CTD profiles from the Weddell Sea south of 70°S and west of 0°. The diagram gives an overview of $\Theta - S_A$ characteristics of the water masses types mentioned in this section. The diagram belongs to Nicholls et al. (2009).

Table 2.1: Overview of the typical properties of water masses found in the Weddell Sea following Daae (2018). The salinity of WSBW and AABW are missing, since they are not defined in the original references. For further references on the values in the table see Daae (2018).

Acronym	Name	Θ [°C]	S_A [g kg^{-1}]
ESW	Eastern Shelf Water	$-1.9 \leq \Theta \leq -1.7$	$S_A < 34.60$
WSW	Western Shelf Water	$\Theta < -1.9$	$34.72 < S_A < 35.00$
WW	Winter Water	$\Theta \sim -1.9$	$34.44 \leq S_A \leq 34.68$
WDW	Warm Deep Water	$0 \leq \Theta \leq 0.8$	$34.80 \leq S_A \leq 34.88$
MWDW	Modified Warm Deep Water	$-1.7 \leq \Theta \leq 0.2$	$34.61 \leq S_A \leq 34.80$
HSSW	High Salinity Shelf Water	$-1.9 \leq \Theta \leq -1.7$	$S_A > 34.81$
WSBW	Weddell Sea Bottom Water	$\Theta < -0.8$	
AABW	Antarctic Bottom Water	$-0.8 \leq \Theta \leq 0$	

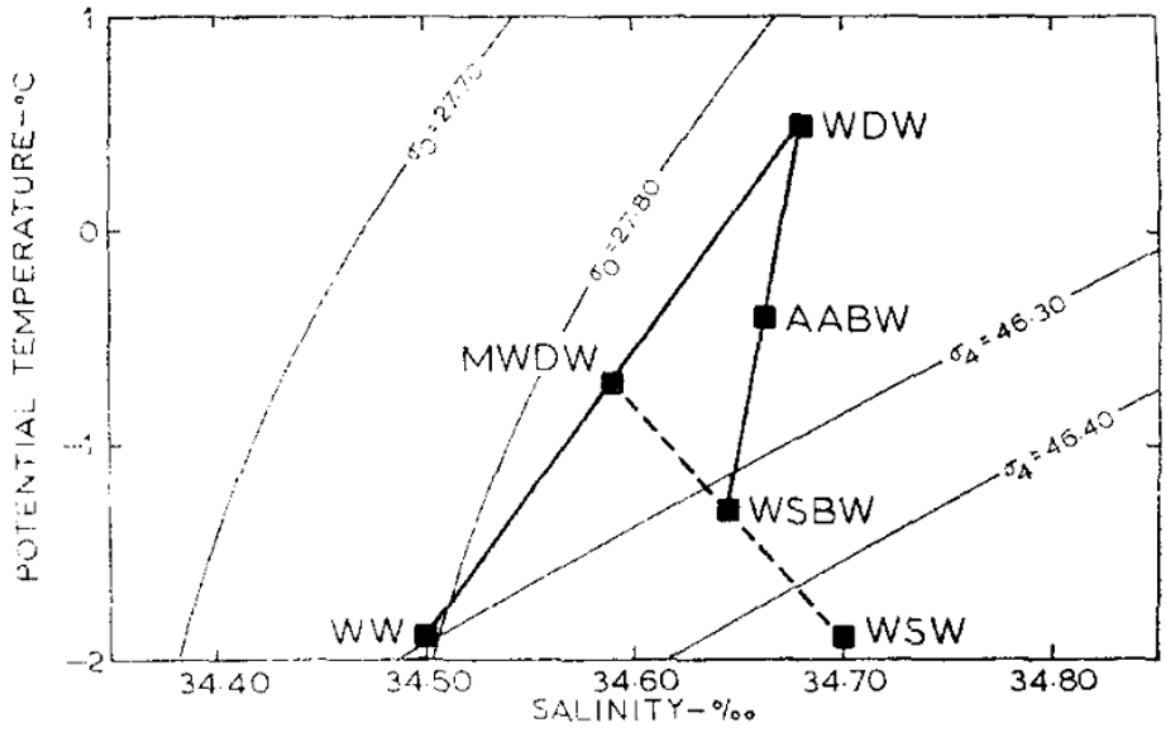

Figure 2.2: Foster and Carmack (1976) showed an idealized mixing scheme on a potential temperature-salinity diagram.

2.2 Antarctic slope front processes

In this section, we present the structure of the Antarctic Slope Current and the mechanisms that act close to the Antarctic continental slope. In the first subsection, we describe the Antarctic Slope Front (ASF) and Antarctic Slope Current (ASC) characteristics. In the second subsection, we pay attention to the mechanisms that drive the variability of the ASC. In the third subsection, we describe the barotropic and baroclinic responses of the ASC.

2.2.1 Definition of Antarctic Slope Front and Antarctic Slope Current

Thompson et al. (2018) shows three different ways to define the Antarctic Slope Front (ASF) around Antarctica's continental shelf and slope. The ASF refers to strong density gradients across the Antarctic shelf break that separates the shelf waters from the offshore CDW (Thompson et al., 2018; Pauthenet et al., 2021). By understanding the mechanisms that drive the structure of the ASF, we can study the contribution of the warm water to the rate of ice shelves melting from below. In addition, the ASF has a strong connection with the ASC, a narrow circumpolar westward flow (Thompson et al., 2018), since horizontal density gradients from north to south support westward currents. Moreover, density gradients intensify the circulation feature over the continental slope. The ASF, accordingly, influences the vertical structure of the ASCs along-slope flow (Thompson et al., 2018), and their strength varies along their path.

The ASF separates the shallow ocean on the continental shelf from the deep ocean. Whitworth et al. (1985) found it from 120°W near the Amundsen Sea and westward to 55°W at the tip of the Antarctic Peninsula. Moreover, characteristics at the front change with changes of the ocean above it due to local melting and freezing and the slope front can meet the upper continental slope (Jacobs, 1991). The ASF, therefore, becomes essential for the exchanges of heat and salt across the continental shelf (Mathiot et al., 2011).

The regions around Antarctica can be divided into three shelf regions: fresh, dense, and warm shelves, while easterly winds with different forces are present. In strong easterly winds (fig: 2.3), an on-shore Ekman transport induces downwelling. Thus, a strong front is built, which separates cold and fresh shelf water from warm and salty offshore CDW. In the case of a dense shelf, the DSW forms in the ice shelf cavity. Therefore, a V-shaped frontal structure modifies both an on-shore transport of the CDW and the export of the DSW from the Antarctic continental shelf. When easterly winds are weak, they can lead to a relaxation of the ASF isopycnals. The CDW, therefore, is possible to reach the ice shelf cavity.

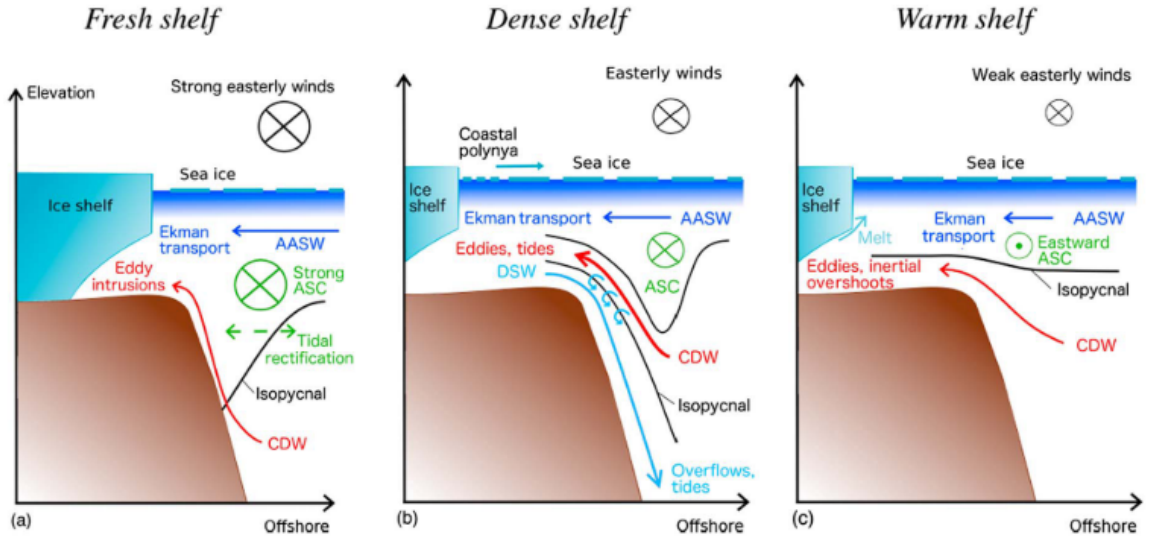

Figure 2.3: Critical water masses, along- and across-slope flows, and supporting mechanisms in the three Antarctic Slope Current (ASC) regimes are described by Thompson et al. (2018): the (a) Fresh shelf, (b) Dense shelf, and (c) Warm shelf.

2.2.2 The variability of the ASF and ASC

Núñez-Riboni and Fahrbach (2009) suggested several mechanisms that contribute to the seasonal variability of the Antarctic coastal current. We associate the Antarctic Coastal Current with the Antarctic Slope Current due to struggling to distinguish them in narrow areas in the Antarctic (Mathiot et al., 2011). Sverdrup transport, thermohaline forcing, thermal wind balance, Ekman transport with along-shore winds, and sea ice drag on the surface affect the transport variability in the ASC (Graham et al., 2013). However, easterly winds drive the dominant direction of the ASC over the Antarctic continental slope (Sverdrup, 1954; Jacobs, 1991; Heywood et al., 2004).

The prevailing easterly winds along the Antarctic continent induce an on-shore Ekman transport. Here, the impact of SIC on the momentum transfer from the wind to the currents is not negligible. Because the SIC modifies the surface drag coefficient, SIC can affect the on-shore Ekman transport. When the ice growth starts, the ice drag decreases until the sea-ice cover reaches its maximum in mid-winter. The drag coefficient has a maximum value when the SIC crosses the 63% line (Núñez-Riboni and Fahrbach, 2009).

The seasonal sea surface height (SSH) variability is related to the seasonality of the wind force (Armitage et al., 2018) that influences the seasonal cycle of the ASC (Mathiot et al., 2011). The ASC is strong in autumn and weak in spring and summer (Armitage et al., 2018). The barotropic current is directly related to the SSH and the baroclinic current links to the Ekman downwelling.

Considering Sverdrup (1954), Núñez-Riboni and Fahrbach (2009) mentioned that the ASC is mainly barotropic due to wind force. Nevertheless, Sverdrup transport contributes to the baroclinic component. The contribution of the barotropic currents (58%) is more substantial than the baroclinic component (18%) due to the wind force (Núñez-

Riboni and Fahrbach, 2009). The baroclinicity is strong in the surface and near the ice shelf (Núñez-Riboni and Fahrbach, 2009). The mechanisms that Núñez-Riboni and Fahrbach (2009) studied, such as Sverdrup transport, sea ice cover, local wind, and thermohaline forcing, contribute to the seasonal variability of the barotropic and baroclinic transports. The mechanisms, additionally, deepen the pycnocline towards the coast and sharpen the baroclinic transport. It shows westward direction at the surface and mid-depth and eastward direction at the ocean bottom and is weaker than the barotropic response. There is stronger response of baroclinic, when the isopycnals are steep.

The barotropic component shows a strong westward maximum in the middle and the end of autumn. In contrast, the baroclinic response is maximum westward in late autumn and spring and minimum in summer. When the zonal wind is maximum in May, the barotropic and baroclinic components of the ASC are also maximum.

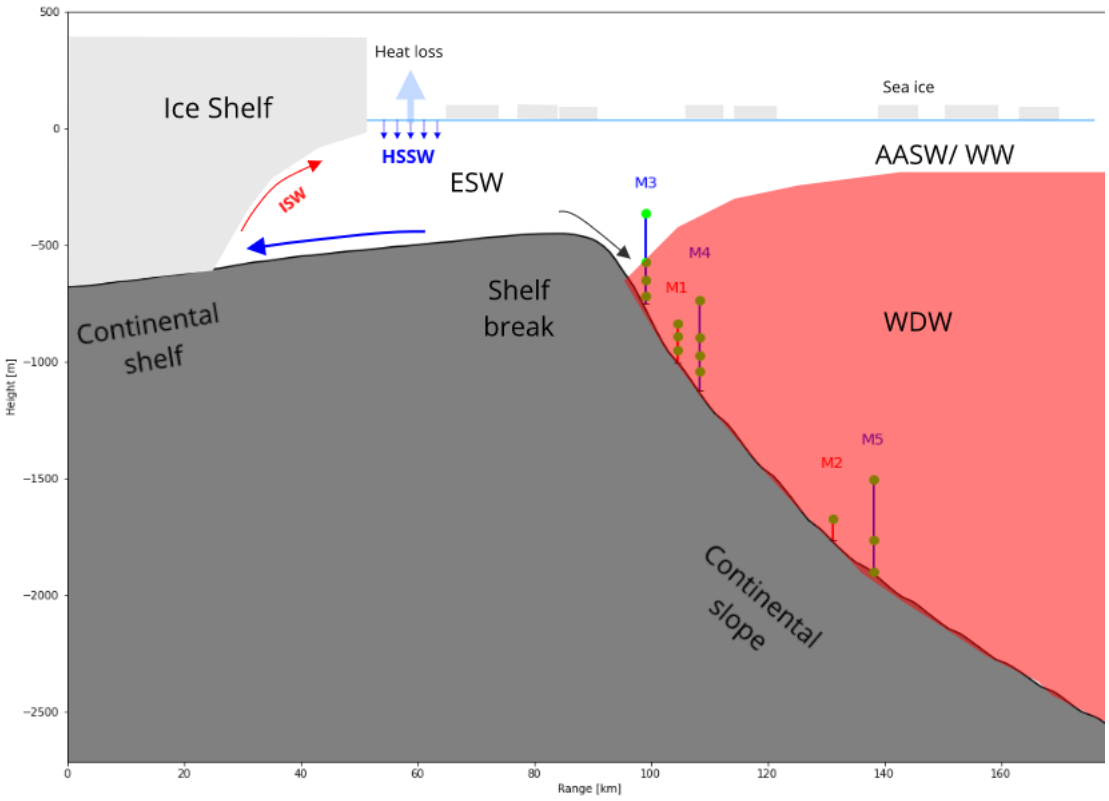

Figure 2.4: Schematic shows the case where the dense shelf water is formed in winter. The blue arrows relate to the formation of High Salinity Shelf Water (HSSW) and its southward transport to the ice shelf cavity. The red arrow shows the ISW, due to the ice shelf melting, caused from mix of the HSSW with the ice shelf meltwater. The black arrow relates to the outflow of dense shelf water across the shelf break. For the bathymetry we use the BEDmap data in the Southeastern Weddell Sea in the eastern flank of the Filchner Trough. The meridional location of the M moorings are indicated. The different colors in M-moorings show two arrays, while green circles show the instruments of salinity and temperature that we use in our analysis. Here, we illustrate the Antarctic Slope Front (ASF).

2.2.3 The mechanisms drive the Antarctic Slope Current

.

The barotropic and baroclinic present a different aspects of the flow's dynamic. For simplicity, we will describe these responses in the fresh shelf region. We first focus on the SSH, where easterly winds along the coast give Ekman transport towards the coast (fig: 2.5). That transports water toward the coast and introduces high pressure onshore and low pressure offshore. Horizontal pressure gradients force the water northward from the high to the low pressure. However, the Coriolis force is not negligible on the rotating Earth, and it deflects the motion and acts perpendicular to the pressure gradients. After the geostrophic adjustment, the current flows westward along the coast and relates to the barotropic response.

In addition, the Ekman transport leads to downwelling near the coast and presses the isopycnals of the ASF down over the continental slope and reflects a westward geostrophic flow (Armitage et al., 2018). Due to the deepening, the surface densities are not aligned with pressure, and a horizontal density gradient is presently leading to pressure differences (fig:2.5). Below the isopycnal, water masses are heavy and relate to the high-pressure system. Water masses are less dense above the isopycnal and connect to a low-pressure system. Pressure gradients, therefore, direct the water southward. After the geostrophic balance, the current flows eastward and relates to baroclinic geostrophic flow. The baroclinic response works against the barotropic one and shows strong currents near the bottom of the isopycnals.

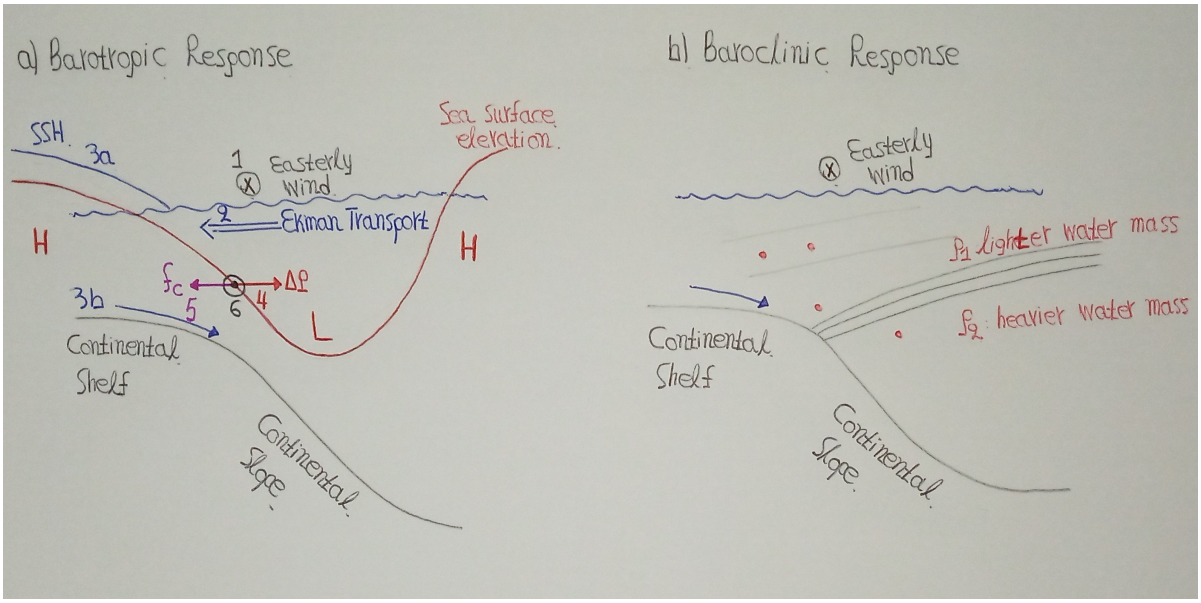

Figure 2.5: Schematic showing the a) barotropic response and b) baroclinic response of the Antarctic Slope Current to the easterly winds along the continental shelf. In the case a) H and L present the high and low pressure system at the ocean due to sea surface elevation. We analyse what happens across the continental slope when easterly winds blow. The Ekman transport (blue arrow) has a southward direction, and the pressure gradients (red arrow) force northward. Then Coriolis (purple arrow) is directed south. a) Barotropic response relates to pressure differences due to sea surface elevation. b) Baroclinic response relates to pressure differences due to density gradients.

2.3 Theory

2.3.1 The ocean surface stress and the influence of sea ice dynamic

When the ocean surface is covered by sea ice, we need to consider the sea ice stress into the ocean surface stress. The sea ice stress is affected by both the ocean current and the wind forces. When the area is fully covered by sea ice, the wind stress cannot move the ice and cannot affect the ocean. However, when the surface water mixes sea ice and open water, the wind stress can affect the ice motion and ocean. By using two different approaches, we can estimate the ocean surface stress. The first approach is the study of surface stress by considering the sea ice motion. Here, we believe the surface stress is due to the ice motion. The second aspect is the study of ocean surface stress without applying a fraction of sea ice. The total ocean surface stress is generally the sum of the surface air stress on open water τ_{ao} and the ice-water stress τ_{iw}. When sea ice is present, it prevents the wind from affecting the ocean directly (Martin et al., 2016). Following Dotto et al. (2018)'s work, we can define the ocean surface stress based on ten-meter wind, ice velocity, and SIC (Dotto et al., 2018). The equation is given by:

$$\overrightarrow{\tau} = \alpha\overrightarrow{\tau_{iw}} + (1-\alpha)\overrightarrow{\tau_{aw}}, \tag{2.1}$$

$$\overrightarrow{\tau_{iw}} = \rho_w C_{diw}|\overrightarrow{U_i}|\overrightarrow{U_i}, \tag{2.2}$$

$$\overrightarrow{\tau_{aw}} = \rho_a C_d|\overrightarrow{U_a}|\overrightarrow{U_a}, \tag{2.3}$$

where $\rho_a = 1.25$ kg $\cdot$ m^{-3} and ρ_w are the densities of air and water. $C_{iw} = 5.50x10^{-3}$ and $C_d = 1.25x10^{-3}$ are the oceanic drag coefficient at the ice-water interface and atmospheric drag coefficient at the open water surface. U_a is the ten meter wind and U_i describes the ice motion.

The surface roughness is related to the air-ice and ice-water drag coefficients, which are affected by the condition of sea ice cover. The surface roughness is low over newly formed ice. When the sea ice covering is low, the wind force has access to the ocean. Thus, more momentum and heat can transfer underneath the sea ice (Martin et al., 2016). However, there are cases where the sea ice can raise the momentum transfer into the ocean compared with the ocean roughness (Dotto et al., 2018). When SIC is around 80-90%, the ocean surface stress reaches its maximum peak, while it is low for 0% and 100% ice covering (Martin et al., 2016).

2.3.2 Ekman transport and pumping

The wind forcing blows parallel to the coastline transfers momentum into the ocean. Easterly winds drive the horizontal circulation along the coast, whereas westerly winds are present further north of the Weddell Sea. In addition, the Ekman transport, generated in the surface layer, moves at 90^o left on the wind stress. The action of Coriolis

forcing and the presence of either a low or high-pressure system can generate the wind's path. As the wind varies spatially, it produces divergence and convergence in the upper ocean layer. Thus, the thermocline is either pushed down or lifted to conserve the mass. The Ekman pumping can explain this, describing vertical velocity in the ocean. The Ekman pumping velocity is given by:

$$W_{EK} = \frac{1}{\rho}\left[\frac{\partial}{\partial x}\left(\frac{\tau^y}{f}\right) - \frac{\partial}{\partial y}\left(\frac{\tau^x}{f}\right)\right], \tag{2.4}$$

W_{EK} is the Ekman pumping velocity, $\overrightarrow{\tau} = \tau^x \overrightarrow{i} + \tau^y \overrightarrow{j}$ is the stress, related to wind and ice-induced stress on the ocean surface and f is the Coriolis parameter. The positive Ekman pumping relates to divergence (upward) transport, while a negative (downward) Ekman pumping relates to convergence transport. These vertical velocities affect both the ASF and the ASC (Thompson et al., 2018; Graham et al., 2013).

Chapter 3

Methods

3.1 Moorings

In 2010, five M-moorings (table: 3.1) were deployed from the University of Bergen (UiB) in the southeastern Weddell Sea $\sim 30^{\circ}$ W, near the Filchner Trough opening (fig:3.2). Details about the M-moorings are given from Jensen et al. (2013). We discuss the quality control of M-moorings in Appendix (chapther: 7). Five other moorings (table: 3.1) belong to the multinational Synoptic Antarctic Shelf-Slope Interactions (SASSI) study in the southeastern Weddell Sea along $\sim 17^{o}$ W (fig: 3.2 and 3.3). Graham et al. (2013) provides more details about the SASSI moored instruments. The five moorings from UiB collected both hydrographic and current velocity measurements, and the moorings from SASSI provided hydrographic. ADCP data are fitted on each of the five SASSI moorings and collected current measurements.

Table 3.1: SASSI mooring and ADCP details. The columns Bottom Depth (m), Height (m) and Instrument are reported to SASSI moorings.

Mooring and ADCP	Time (UTC)(in/out)	Position (lon/lat)	Bottom Depth (m)	Height (m)	ADCP depth (m)	Parameter	Instrument
SASSI1	02 Feb. 2009	$17^{0}27'45''W$	273	256	132-244	C,T,P,U,V	SBE 37
	24 Feb. 2010	$72^{0}29'10''S$					
SASSI2	01 Feb 2009	$17^{0}37'41''W$	487	449	40-424	C,T,P,U,V	SBE 37
	24 Feb. 2010	$72^{0}27'28''S$					
SASSI3	01 Feb 2009	$17^{0}43'12''W$	973	467,963	40-424	C,T,P,U,V	SBE 37
	24 Feb. 2010	$72^{0}26'24''S$					
SASSI4	01 Feb 2009	$17^{0}01'05''W$	1600	405	40-376	C,T,P,U,V	SBE 37
	25 Feb. 2010	$72^{0}25'00''S$					
	01 Feb 2009			1572		C,T,P	SBE37
	05 Oct 2009						
SASSI5	25 Feb 2009	$18^{0}37'55''W$	2600	478,980 1943,2578	40-424	C,T,P,U,V	SBE 37
	25 Feb 2009	$72^{0}15'10''W$					

All the moorings from M and SASSI are located across the Antarctic continental shelf and slope in the southern Weddell Sea from 2009 to 2010 (fig: 3.2). In southeastern Weddell Sea, two arrays give two paths across the continental slope. The first array consists of the moorings M1 and M2 approximately in the middle of the Filchner Sill. The second one is located 80 km east and combines the moorings M3, M4, and M5.

Figure 3.1: Mooring summary data provided from Jensen et al. (2013).

Table 1. Mooring Details[a]

Mooring	Time (UTC) (in/out)	Position (lon/lat)	Bottom Depth (m)	Height (m.a.b.)	Parameter	Instrument
M1	10 Feb 2009	32°19′12″W	967	10, 67	*T, C*	Microcat
	17:39	74°13′41″S		24	*T, C, V*	RCM-7
				46	*T, P, V*	Aquadopp
	10 Feb 2010			87	*T*	SBE 39
	22:00			123	*T, C, P*	Microcat
				136	*T, P*	SBE 39
M2	11 Feb 2009	32°16′41″W	1898	19	*T, P, V*	RCM-7
	18:05	73°58′41″S		68	*T*	SBE 39
				114	*T, C, P*	Microcat
	10 Feb 2010			156	*T, P*	Sentinel
	22:00			78:4:150	*V, W*	Sentinel
M3	13 Feb 2009	30°09′54″W	725	10	*T, C*	Microcat
	16:30	74°30′38″S		25	*T, V*	RCM-7
				77, 154, 360	*T, C, P*	Microcat
	9 Feb 2010			102, 128, 257	*T*	SBE 39
	18:00			123:4:199	*V, W*	Sentinel
				205	*T, P*	Sentinel
				308	*T, P*	Continental
				310:5:505	*V, W*	Continental
M4	13 Feb 2009	30°02′38″W	1051	9, 78, 314	*T, C, P*	Microcat
	13:19	74°26′17″S		25	*T, V*	RCM-8
				104	*T*	SBE 39
	9 Feb 2010			156	*T, C*	Microcat
	15:00			183, 261	*T, P*	SBE 39
				419	*T, P*	Longranger
				442:16:986	*V, W*	Longranger
M5	12 Feb 2009	29°32′36″W	1917	10, 415	*T, C*	Microcat
	22:43	74°10′09″S		26	*T, C, V*	RCM-7
				52, 104, 311, 363	*T*	SBE 39
	10 Feb 2010			78, 259	*T, P*	SBE 39
	22:00			155	*T, C, P*	Microcat
				415	*T, P*	Longranger
				55:16:391	*V, W*	Longranger

[a]*T* is temperature, *C* is conductivity, *P* is pressure, *V* is horizontal velocity, and *W* is vertical velocity.

The two arrays in M-moorings are roughly found at same isobath on the continental slope. More specifically, M1 and M4 are at about 1000 m isobaths, and M2 and M5 are at 1900 m. The mooring M3 was deployed at the continental shelf 9.3 km south of the M4 (fig: 1.1).

In the SASSI-moorings, one array presents the path across the shelf and slope. The moorings SASSI1 and SASSI2 are above the 500 m isobath along the continental shelf. The moorings SASSI3, SASSI4, and SASSI5 are above 1 km, $\sim$1.5 km, and $\sim$2.5 km isobaths. They give details along the continental slope. The distance between the shallowest mooring on the shelf SASSI1 and the deepest offshore mooring is approximately 50 km (Graham et al., 2013).

From the SASSI-area, we get information about the currents by using acoustic Doppler current profilers (ADCPs; RDI) above 500 m (fig:3.3). The ADCP data are fitted on each of the five SASSI-mooring (Graham et al., 2013). In the following analysis, we will refer to the currents as SASSI currents.

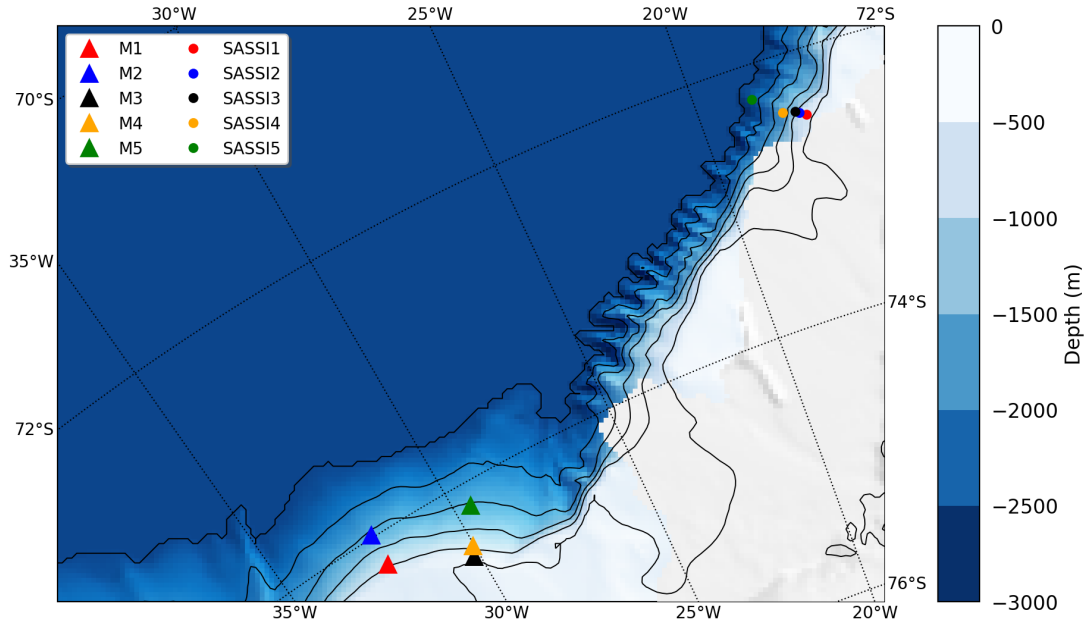

Figure 3.2: Showing the location of the M and SASSI moorings in the Southeastern Weddell Sea. Isobath contour lines (Fretwell et al., 2013b) are shown at -1000, -1500, -2000, -2500 and -3000 m (black lines). We show the land and floating ice shelf in light gray.

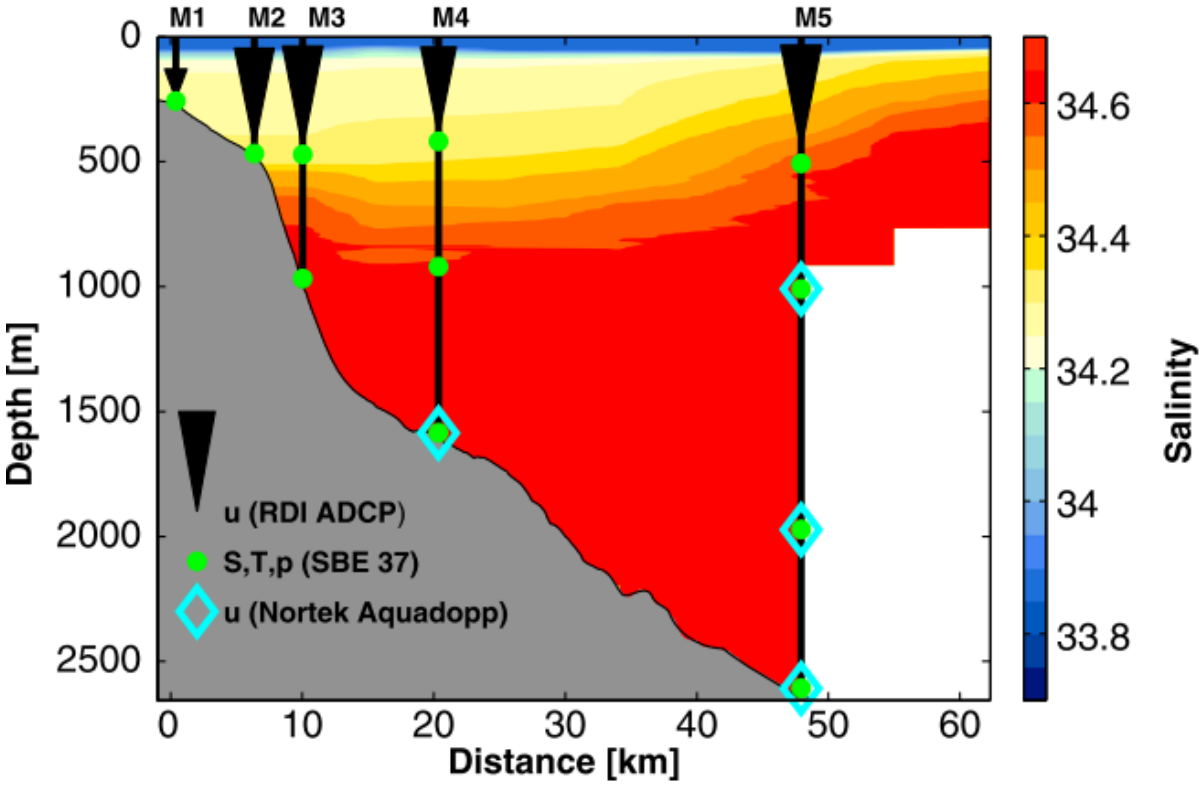

Figure 3.3: A schematic for the cross section of the moorings showing the depth of the instruments. It shows the location of ADCP, SBE-37, and Nortek Aquadopp instruments on each of the five moorings. Colored contours present the salinity section during February 2009. The figure belongs to Graham et al. (2013).

3.2 Currents direction from mooring data

We present the currents direction from average depths of daily observation data. In the M3 526-602 m and M4 513-609 m, we see that the currents flow towards WNW with an average direction 55°. In the SASSI1 132-244 m and SASSI3 40-424 m, the currents flow towards SWW with an average direction of the mean flow 114° and 124° respectively. For the time series analysis of the currents, we rotate the currents. For the M, we use only the current data from M3 and M4, and we rotate them by 55°. For the SASSI, we rotate each ADCP data regarding to their average direction. In the table 3.2, we present the exact angles that we use.

Table 3.2: The average direction of the mean flow in SASSI currents

Current	Mean direction
SASSI1 132-244 m	114°
SASSI2 40-424 m	119°
SASSI3 40-424 m	124°
SASSI4 40-376 m	128°

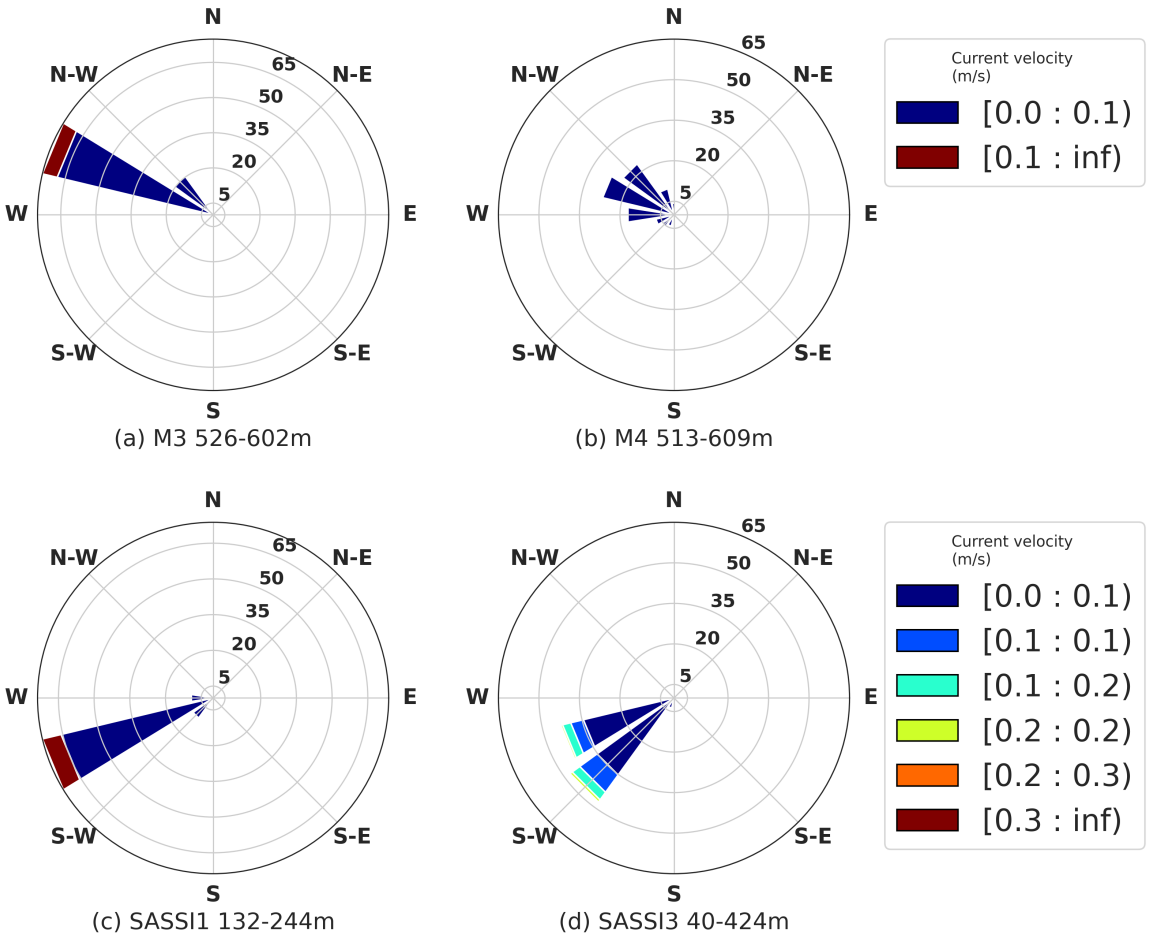

Figure 3.4: The rose plots show the direction of the currents in average depths in a) M3 and b) M4, where we find hydrostatic instuments. c) and d) show the direction of the currents from ADCP data in SASSI1 and SASSI3. Each rose plot describes the current by class and direction. In the legend, each line presents velocity class and each column presents a current direction class.

3.3 Additional datasets

This section provides information about the bathymetric data, current velocity measurements from ADCP observations, and atmospheric data used to calculate drag coefficient and ocean surface stress.

3.3.1 Bathymetry from Bedmap2

The product of Bedmap2 is produced by the British Antarctic Survey (BAS), which presents good aspects of Antarctica's dathymetry (Fretwell et al., 2013a). Bedmap2 consists of the ice thickness and subglacial topographic model of Antarctica. Moreover, it provides details of surface elevation, ice thickness, and the seafloor and sub-glacial bed elevation of the Antarctica south of 60° S (Fretwell et al., 2013a). The ice thickness, bed, and surface elevation have a uniform resolution of 1-km spacing. The BAS uses data from different sources to improve the original Bedmap version (Bedmap1). In the Bedmap2, 25 million measurements constructed the ice thickness grid (Fretwell et al., 2013a). The sub-glacial landscape is much better visible in most parts of Antarctica than the Bedmap1 presented. With the new version of Bedmap, we can analyze the bed below the Antarctic ice sheet in much greater detail. The several datasets of Bedmap2 are a collection of radio-echo-sounding measurements, seismic techniques, satellite readings, and cartographic data (Fretwell et al., 2013a). To create the maps of Antarctica, we use a code from Elin Darelius.

3.3.2 Atmospheric forcing from ERA5

The European Centre for Medium-Range Weather Forecasts (ECMWF) produces the reanalysis ERA5 (Hersbach et al., 2020). The ECMWF provides a reanalysis of the global climate and weather. The ERA5 reanalysis uses a combination of observations and model data to produce an estimation of the atmosphere. ERA5 provides global hourly data with an uncertainty estimation of three hours from 1979 up to today (Hersbach et al., 2020). These uncertainties are associated with the available observations in sensitive areas. The horizontal resolution of ERA5 has a regular lat-lot grid of 0.25 degrees and an uncertainty estimate of 0.5 degrees (Hersbach et al., 2020). We use daily SIC, ten-meter wind, and SLP data from ERA5 from 2008 to 2010. For the estimation of wind forcing, we use its zonal and meridional components at 10 meters above the surface of the Earth in meters per second. The u-component is the horizontal speed of the air moving eastward, and the v-component moves towards the north. The SIC provides information on the sea ice-covered occurring in grid boxes. Although each grid box includes ocean or inland water, the ERA5 does not give details of ice that forms on land like glaciers (Hersbach et al., 2020). The dataset of SIC provides data alog the coast (fig. 3.2). Since we're interested in mesoscale variability, we average the hourly data into daily means.

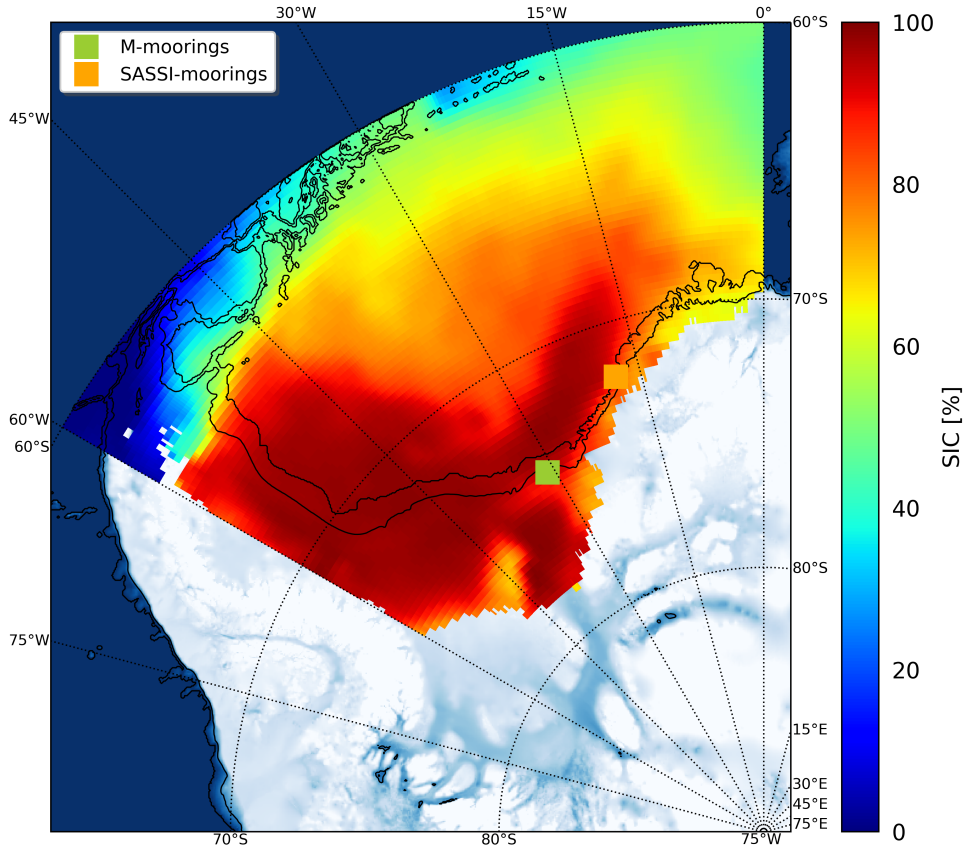

Figure 3.5: The map shows the yearly average dataset of SIC from ERA5 in the Weddell Sea in 2009. From the datasets of BEDMAP (Fretwell et al., 2013b), we present the land and a floating ice shelf in light gray. Black lines are isobaths at 2000 m and 3000 m depth. The SIC was extracted from latitude [60°S, 80°S] and longitude [60°W, 0°W]. The colorbar shows the yearly average SIC. We also present the position of the M−moorings (green) ∼ 30°W and SASSI−moorings (orange) ∼ 17°W in the Weddell Sea.

3.3.3 Rotation of ERA5 and moorings

In addition, the rotation of wind force and currents are demanding. Here, we decided to rotate the wind in the SASSI area along the slope and the currents along with the average direction of the mean flow that each mooring shows.

Although we get information on the zonal and meridional wind components, we are interested in knowing the wind components along and across the slope. Thus, we should rotate the coordinate system. In the M-box (∼ 30°W), the coordinate system is parallel to the topography. The topography shows a steep incline in the SASSI-box (∼ 17°W). Considering Graham et al. (2013), we need to rotate the wind vectors clockwise by 139°. We use the same angle in M-area.

In figure 3.6 we present a simple example behind the definition of the rotation of a wind vector. While the angle increases counterclockwise, the positive angle is on clockwise rotation. From ERA5, the daily average u- and v-wind field components give different signs and wind vectors. When we rotate the wind, wind flow along y' will be the along slope wind with positive values indicating flow towards 229°. The wind along

x' will be the across-slope wind with positive flow off-shore towards 139°. In the case of currents from M-moorings and ADCP from SASSI-area, we decide to rotate the coordinate system, where we use as an angle the mean direction of the depth-average current from each ADCP and M-moorings. For the rotation of the coordinate system, we apply the following equations:

$$x' = x \cdot \cos(angle) + y \cdot \sin(angle) \tag{3.1}$$

$$y' = -x \cdot \sin(angle) + y \cdot \cos(angle). \tag{3.2}$$

We assume that the y' is along the slope, and the x' is across the slope.

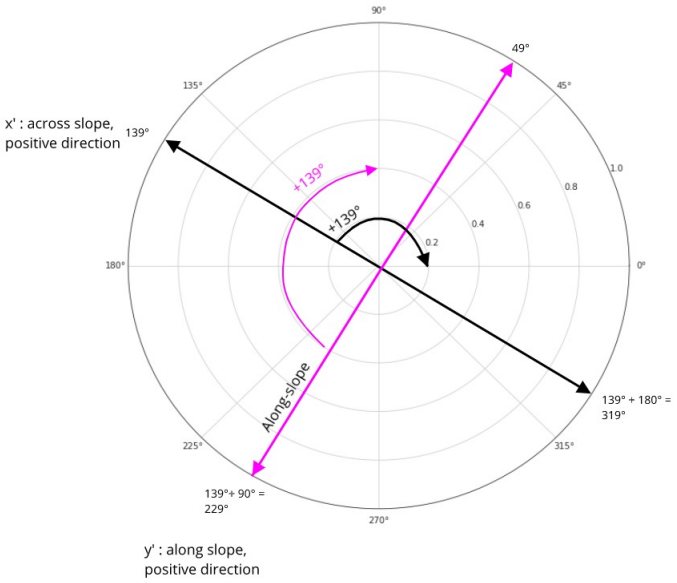

Figure 3.6: It shows the XY-Cartesian coordinate system with angles. It also presents the direction of the wind vector (black arrow), the location of the along-slope (pink arrow), the wind vector after rotation (blue arrow), and the new $x'y'$ Cartesian coordinate system.

3.3.4 Sea ice motion

The direct calculation of ocean surface stress is challenging. It depends on measurements of ocean currents, surface roughness, and sea ice strength that varies spatially (Andreas et al., 2010). However, we can estimate the ocean surface stress through a parametrisation. Here, we estimate the ocean surface stress by following Dotto et al. (2018), and Andreas et al. (2010). The wind stress on open water and the stress due to sea ice are components of the ocean surface stress separately. Since Dundas (2019) use four different estimations of ocean surface stress and find that their differences are low, we decided to use just the methods from Andreas et al. (2010) and Dotto et al. (2018). We should consider that the presence of sea ice can adjust the stress from the atmosphere into the ocean. Therefore, we should keep in mind that fast ice can block the effects of wind stress on the ocean surface. If the sea ice is moving, it changes

the momentum transfer. The parametrisations agree with each other, although they represent the impact of sea ice on surface stress differently, Andreas et al. (2010)'s parametrisation, the sea ice dynamic is not considered directly, but the drag coefficient includes a dependency on the SIC parametrizing the ice movement. From Dotto et al. (2018)'s model, we estimate the ocean surface stress by considering the sea ice movement. While the model does not consider the ocean movement itself, Dotto et al. (2018) presents a realistic overview of ocean surface stress. We give more details for these two parametrizations in the following section.

To study the surface stress due to sea ice movement, we need to use data on ice motion. For this purpose, Vår Dundas helped us to download the data-set of ice motion at the same areas, where we use ERA5 (fig:1.1) and calculate the ocean surface stress from the Dotto et al. (2018)'s method. We use data of ice motion from the National Snow and Ice Data Center (NSIDC). The NSIDC grids the data-set on a cartesian coordinate system and uses the 25 km Equal-Area Scalable Earth (EASE) Grid. Since the data sets from the ERA5 are oriented on a grid based on latitudes and longitudes, we need to transfer the data-set of ice motion onto the lat-lon projection. Dundas (2019) provides more details about this dataset in her work.

3.4 Parametrisation of drag coefficient Cd

For simplicity, we use the parameterisation of ocean surface stress as was provided Andreas et al. (2010). Here, we decide not to consider new sea ice motion, and thus, we use only the dataset of SIC given from ERA5. Andreas et al. (2010) immitate the ice motion through the drag coefficient, which changes with varying sea ice concentration.

The drag coefficient generally depends on the wind speed and the stratification. For simplicity, we assume neutral stratification in the atmosphere to avoid the effects of the heat flux in the atmospheric boundary layer. In a neutral stratification, where both leads and melt ponds are present, we study the sea ice and open water with a drag coefficient at 10 m height from the surface. Lüpkes and Birnbaum (2005) was the first to explain drag coefficient behaviour in the marginal ice zone. Their parametrisation needs the information of the ice freeboard, the size of the ridge, the width of floes, and the open water distance between floes. Due to the impractical application of the model, they simplify the prediction of drag coefficient as a function of ice concentration:

$$10^3 C_{DN10} = 1.500 + 2.230 C_i - 2.333 C_i^2, \tag{3.3}$$

.

where C_i is the sea ice concentration.

In the drag coefficient C_{DN10} Andreas et al. (2010) avoid applying the ice dynamic and only use the wind force. This parametrisation considers that the drag coefficient increases with the rise of sea ice covering until 0.4. Up to 0.4, the drag coefficient decreases with the increases in SIC.

3.5 Ekman pumping velocity and Ekman pumping

One of the main goals is to study the connection between the Ekman pumping and the mesoscale variability of the ASF.

To simplify the estimation of Ekman pumping velocity, we assume that f is constant because its changes are small on the spatial scales. We, therefore, ignore the β-effects.

In the standard coordinate system, an expression of the Ekman pumping velocity is given by:

$$W_{EK} = \frac{1}{\rho}\left[\frac{\partial}{\partial x}\left(\frac{\tau^y}{f}\right) - \frac{\partial}{\partial y}\left(\frac{\tau^x}{f}\right)\right], \tag{3.4}$$

$$W_{EK} \approx \frac{1}{\rho f}\left[\frac{\partial \tau^y}{\partial x} - \frac{\partial \tau^x}{\partial y}\right]. \tag{3.5}$$

3.6 Data analysis

This section gives an overview of data analysis: 1) spectral analysis, 2) low-pass filtering, and 3) correlation analysis.

3.6.1 Spectral Analysis

To study the variability of time series data, we apply spectral analysis. It shows the variance of a time series as a function of frequency that its mean and trend are removed (Thomson and Emery, 2014a). The spectral analysis is based on the Fourier transform study, where we can define a periodic signal in the data set. Time series from observational data sets have a limited duration T=NΔt, where Δt is the sampling interval, and N is the total number of data points (Thomson and Emery, 2014a). According to Fourier transform analysis, a periodic variable can be described as a function of sines and cosine components.

$$y(t) = \bar{y}(t) + \sum_{p} [A_p \cos(\omega_p t) - B_p \sin(\omega_p t)]. \tag{3.6}$$

The equation is called Fourier analysis, where $\bar{y}$ is the mean value of the record, and A_p and B_p are the Fourier coefficients. The p represents the limited number of Fourier components, p = 1, 2, ..., N/2. This number takes into account the highest frequency f_N=1/2Δt that we can find and the Rayleigh's criterion, in which f_0= 1/NΔt describes the limit of frequency resolution (Thomson and Emery, 2014a). In addition, ω_p=2πp/T is the angular frequency of the fundamental frequency $1/T$, where T is the total length of the time series. The Fourier coefficients are calculated by:

$$A_p = \frac{2}{N} \sum_{n=1}^{N} y_n \cos(\frac{2\pi pn}{N}), \tag{3.7}$$

$$B_p = \frac{2}{N} \sum_{n=1}^{N} y_n \sin(\frac{2\pi pn}{N}), \tag{3.8}$$

$$A_0 = \frac{2}{N} \sum_{n=1}^{N} y_n, \tag{3.9}$$

$$B_0 = 0, \tag{3.10}$$

where y_n is the contribution from the nΔt data values. This method helps us identify periodic components in time series. The power spectra density (PSD) shows the energy per unit frequency. The peaks in the PSD graph indicate the frequencies of dominating variability

Each raw spectra without window has N values and gives two degrees of freedom (DoF) (Thomson and Emery, 2014a). The DoF corresponds to the magnitude and phase of

each Fourier component. For having a reliable estimation of the raw spectra, we smooth the time series through the Hanning window that minimises leakage in the spectral domain. While the Hanning window increases the degrees of statistical reliability per spectra, the frequency resolution is reduced. The periodogram smoothing is achieved through convolution, and it has a smaller length than the length of the raw spectra (Thomson and Emery, 2014a). Applying the Hanning window, we split the original time series into short overlapping segments. While smoothing each short time series, we use 50% of overlapping.

In our case, we should be careful when deciding a segment length. Our goal is to notice similar periodicity between the water masses and the wind force. For this purpose, we group the hourly mooring data into daily getting 365 data points, while we get 1096 data points from 3 years ERA5 data. By studying the significance of the frequency spectra of both water masses and wind forces, we find that an appropriate segment length is four months when applying a Hanning window. To check whether the spikes in the frequency spectra have physical meaning, we study the significant levels of each frequency (Thomson and Emery, 2014a). The significant levels define the degrees of certainty that we find a frequency between specified lower and upper bounds of the estimated parameter. A typical significance level is 0.05, in which 95% is contained between the points.

3.6.2 Low-pass Filtering

By studying the variability of the water masses, we can determine the signal of mesoscale variability. We study the daily averages of data from the moorings. Commonly, devices are not perfect, and thus, background noise or instrumental errors can appear in the mooring data. Due to that, we want to avoid the signal from tidal forcing, we apply a low-pass filter.

A good low-pass filter depends on five qualities: 1) a sharp cut-off where unwanted high-frequency components are removed effectively, 2) a comparatively flat passband leaving the low-frequency components unchanged, 3) a clean transient response, 4) zero phase shift, and 5) acceptable computational time (Thomson and Emery, 2014b).

There is some limitation of frequency in window filters (Thomson and Emery, 2014b). More specifically, the maximum range of frequencies in a digital filter is identified by the Nyquist frequency $f_N = 1/2\Delta t$, which is the highest detectable frequency. It is also determined by the fundamental frequency $f_0 = 1/N\Delta t$ described as the lowest detectable frequency. Thus, the digital filter is applied on the frequency range $f_0 < f < f_N$.

In this method, we apply a 4th-order Butter-worth filter with a 15-day cut-off frequency, where we leave the low-frequency components undisturbed.

3.6.3 Correlation Analysis

Our goal is to explore what drives the variability at moorings along the continental shelf and slope in the Southern Weddell Sea. We, therefore, want to know which the parameters influence each other. For this purpose, we apply the correlation analysis estimating the co-variance of time series (Thomson and Emery, 2014a). If we consider two random variables, X and Y, their correlation coefficient r_{XY} is given by:

$$r_{XY} = \frac{1}{N-1} \sum_{i=1}^{N} \frac{(X_i - \overline{X})(Y_i - \overline{Y})}{\sigma_X \sigma_Y}, \tag{3.11}$$

where X_i and Y_i are the discrete parameters of the time series X and Y, $\overline{X}$ and $\overline{Y}$ are the mean values of X and Y. σ_X and σ_Y represent the standard deviation of X and Y.

The resulting coefficient has a range between -1 and +1 (Thomson and Emery, 2014a). In the case of r= $+1$, the samples show a perfect linear correlation, and X rises when Y rises. In the case of r= -1, they have a perfect negative linear correlation, and X increases when Y decreases. For r= 0, the variables do not relate. While two time series co-vary and show a high correlation, this does not necessarily mean that the variation in one parameter is the cause of the variation in the other one.

While we do a lag correlation analysis in a low-pass filter observational data, we must check the p-values that show the statistical significance of the lag correlation. When the p-values is less than 0.05, there is a statistically significant association between the two variables.

Chapter 4

Results

4.1 Wind force and the surface stress parametrisation

Wind roses from the M area and the SASSI area (fig: 1.1), show the average daily wind direction and speed (fig: 4.1). Generally, the wind rose acts as a histogram bar chart. The circumpolar format of the wind rose shows the direction of the wind, and the radius shows the frequency of each direction.

The wind mainly blows from the southwest and northeast over 8-10% of the time in the M area. A direction from the northwest and southeast frequency is 4% (fig: 4.1). The most extended radius in the southwest and northeast shows a wind speed between 9-13 m/s with a frequency of over 10%. Also, the wind that blows from northeast and southwest has a speed scale of 13-17 m/s, about 8% over time. The wind in the SASSI area is blowing similarly to the wind in the M area, where their wind directions align. The significant wind blew from northeast and southwest over 10-12% over the time. The wind does not often blow from southeast and northwest with a frequency of around 4% and speed between 1-5 m/s. It shows a higher speed between 17-21 m/s, about 11%, than in M-area.

As we described in the section 2.3.1, the calculation of surface stress is challenging due to the sea ice cover. In the beginning, we calculate the surface stress by Andreas et al. (2010)'s parametrisation, imitating the effect of sea ice motion through the variation of drag coefficient responding to the variability of SIC. The sea ice affects the surface stress and the interaction with the ocean underneath in observing M-moorings and SASSI-moorings. For this purpose, we have also decided to provide details of surface stress while we directly use the sea ice motion from the ice-water stress. In the figure 4.2 we introduce the two methods of the total surface stress average of the M-area ($\sim 30 \circ W$). For simplicity, we recall τ_{ice} the ocean surface stress following the equation 2.1 from Dotto et al. (2018). As τ_{Cd}, we identify the surface stress following the parametrisation of drag coefficient from Andreas et al. (2010) (eq: 3.3).

We apply low-pass filtered daily mean datasets from ERA5 over three years. From 2009 to 2010, when mooring datasets were available, the sea ice-covered was 100%, signifying the presence of sea ice the whole year. Comparing the total surface stress in M-area, we notice how similar the stresses vary. We find low differences between

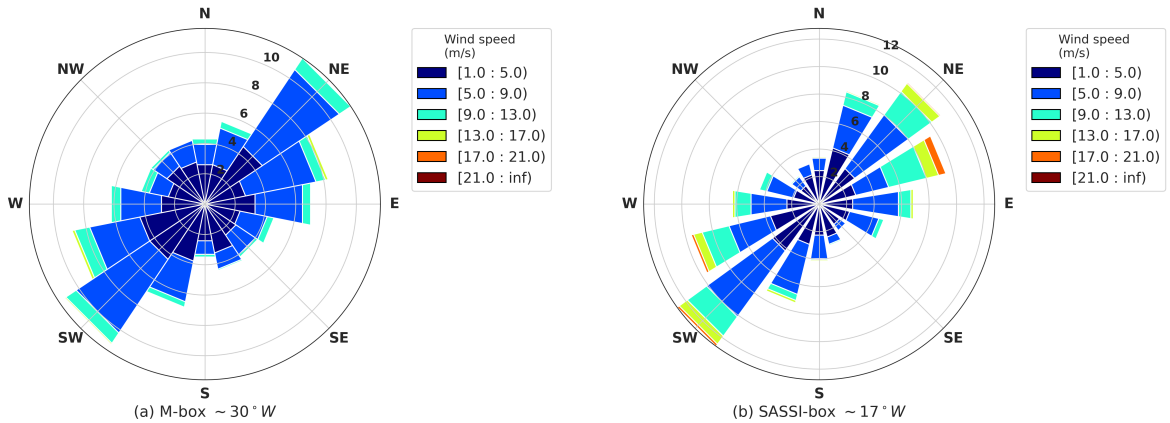

Figure 4.1: The wind field components find the wind direction from ERA5 during the period we have mentioned in the section 3.3.2. To find the wind direction at a) $\sim 30°W$ and b) $\sim 17°W$, we use windrose diagram. It describes the wind speeds by class and direction. In the legend, each line represents a wind speed class and each column represents a wind direction class.

the variation of τ_{Cd} and τ_{ice} (fig: 4.2). When we do not consider the ice motion, the surface stress (τ_{Cd}) shows higher peaks than τ_{ice}. When we apply the ice motion into the surface stress (τ_{ice}), the stress shows lower peaks than τ_{Cd}. These two different methods seem to agree with the calculation of along flow surface stress. When the SIC is almost 100%, they present similar variation and magnitudes over M-area. Same results we find on the total surface stress in the SASSI area, which we do not contribute there. We expect to see the greatest differences in the stress parametrisations when there is a medium amount of sea ice. Therefore, it is most mobile and affects the stress most strongly. In the figure 3.5, we present the daily average SIC without filter during the mooring observations in the Weddell Sea. We notice that SIC is 100 % approximately in the areas close to the continental shelf. The SIC is low farther north and east in the Weddell Sea.

In the following analysis, we will use only the parametrisation of Andreas et al. (2010). The sea motion is dependent both on currents and wind force. During winter, when the SIC is almost 100%, the τ_{ice} follows the variability of τ_{Cd}, in which we use only the wind force. Therefore, the wind force drives the sea ice that does not stuck. While the slight differences between the parametrisations are not negligible, Andreas et al. (2010) gives a good overview of surface stress without needing to apply many variables. To compare the total surface stress between the two areas, we confirm our conclusion in the figure 4.1. The entire surface stress in the SASSI area presents the same variability as in M-area. However, the surface stress is two times stronger in SASSI-area than in M-area during winters. We apply frequency spectral analysis to a better estimation of the differences between the M and SASSI.

The frequency spectral of the non-filtered daily total surface stress from M and SASSI areas is shown in figure 4.3. It shows significantly higher energy levels in SASSI than M, confirming our discussion before. Looking at the significance of peaks that originated from the Hanning window with a segment length of four months, we find that low peaks do not show a physical meaning in the M area. While the frequency spectra at the SASSI area has a physical sense, the surface stress does not present any signal

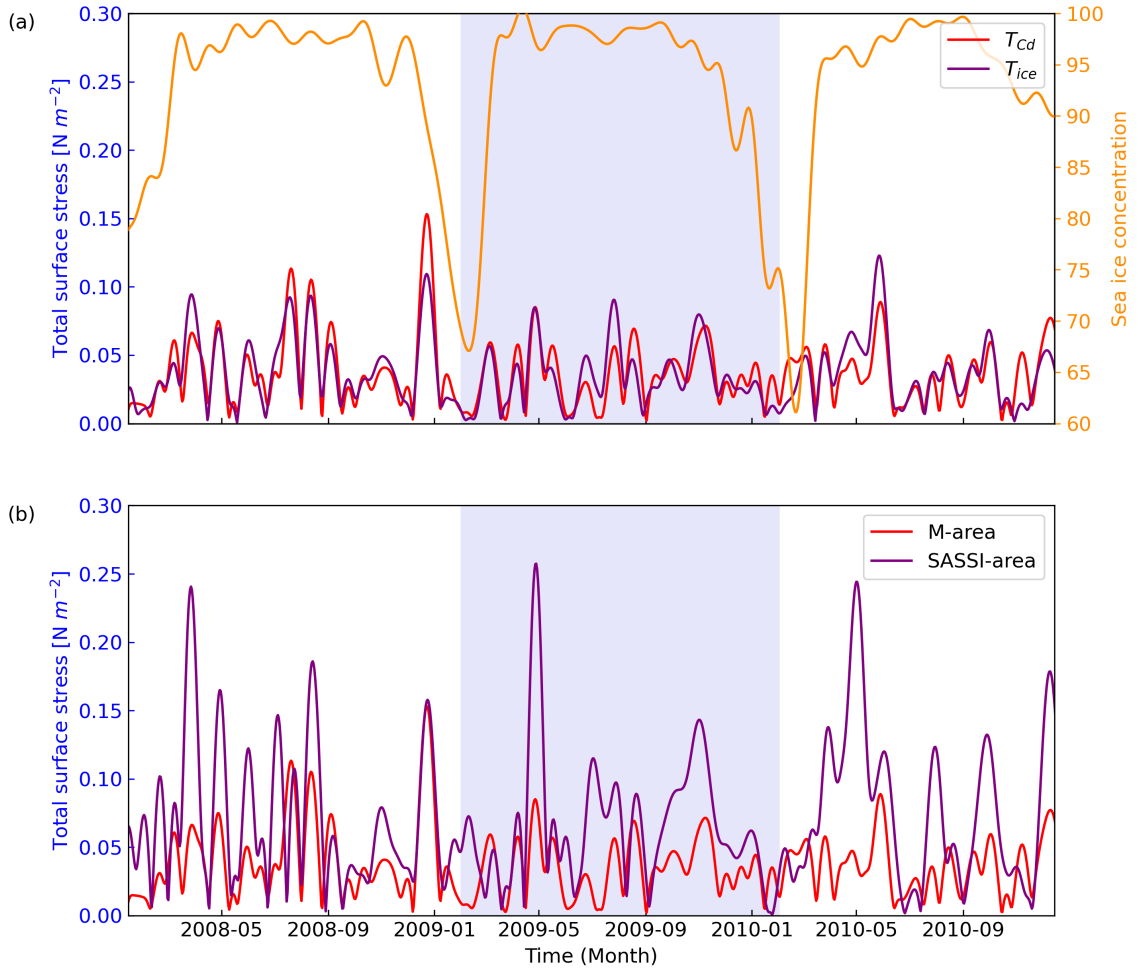

Figure 4.2: Low-pass filtered (15-days) daily mean total surface stress [N m^{-2}] (a) over the M-area using two different methods for studying the surface stress, and (b) over the M and SASSI-area, where we apply the parametrisation of Andreas et al. (2010). The rectangle (light grey) represents the period of moorings. The τ_{Cd} (red) is based on the parametrization of Andreas et al. (2010) and τ_{ice} (purple) based on Dotto et al. (2018). In (a), we refer to the two parameterisations on the left vertical label (blue) and the SIC on the right vertical label (dark orange). In (b), we refer to the total surface stress in the M area (red) and SASSI area (purple) on the left vertical label (blue)

in the mesoscale variability. In Appendix (chapter: 7) we further analyse the frequency spectra between the atmospheric forcing and the currents in specific depths.

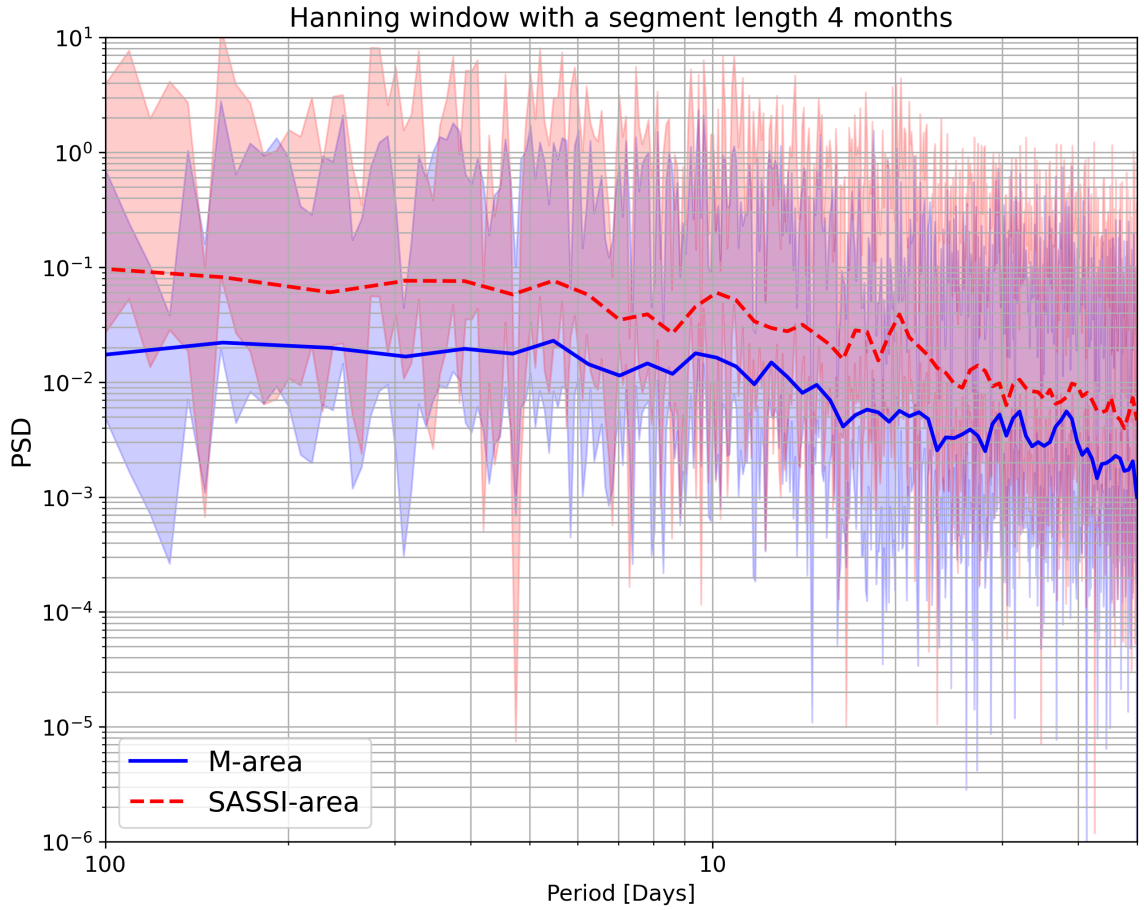

Figure 4.3: It shows the frequency spectra from non-filter daily averaged total surface stress in the M and Sassi areas. The blue and red overshadow ranges present the significant levels of raw spectra with two Degrees of Freedom (DOF) at the M and SASSI areas, respectively.

4.2 Mooring observations

This section presents the characteristics of the water masses from M moorings and SASSI moorings along the continental slope. We also give information about their variabilities by applying a low-pass filter of daily hydrography and currents with a frequency cut of 15 days. We use ADCP data above 400 m depth in the SASSI study.

4.2.1 Characteristics of water masses

We typically observe the water masses according to their TS properties. In the M-area ($\sim 30^{\circ}W$), the water masses are mainly MWDW, but WDW and ESW are also present the whole year (fig: 4.4). Warmer and saltier water masses are located at a greater depth and further offshore on the slope. Moreover, we typically find WDW at 2000 m depth with maximum salinity 34.85 $g \cdot kg^{-1}$ and range of temperature [0, 0.40] ^{o}C. The WW appears at the shallowest instrument's depth, M3 - 365 m and M3 - 571 m, located between the shelf and slope. Their minimum temperature, close to the freezing point, mainly shows this kind of water mass. In a deeper depth, M-moorings mostly show MWDW that lies on the mixing line between WW and WDW. Not only do we see MWDW, but we also find WDW and ESW.

In the SASSI-area ($\sim 17^{\circ}W$), the shallowest moorings, SASSI1 and SASSI2, are close to the continental shelf. Both are close to the freezing point and dominated by WW (fig: 4.5). In June 2009, they show a low temperature at roughly $-2^{\circ}C$ and low salinity varying from 34.25 to 34.5 $g \cdot kg^{-1}$ in SASSI1 and from 34.4 to 34.5 $g \cdot kg^{-1}$ in SASSI2. Every month, the water masses shift their characteristics. Moreover, they seem to become saltier and warmer, but their temperature does not overcome $-0.5^{\circ}C$ with density at 27.76 $g \cdot kg^{-3}$. The SASSI3 and SASSI4, along the slope, present MWDW. The SASSI5, offshore the continental slope, shows saltier and warmer water masses that do not shift their characteristics. The estimation of seasonal changes in water masses are difficult to explain from the $\Theta - S_A$ diagrams since they often vary. Only the water mass in M2 - 1898 m, M3 - 365 m, and M5 show a shifting of their characteristics. More specifically, the water mass becomes saltier in M2, while the water mass in M3 - 365 m is saltier and is closer to the freezing point. The water masses in M5 show a low shifting, while the range of salinity and temperature remain the same the whole year.

Changes in the surface stress forcing and the Ekman pumping anomaly are expected to influence the strength of the ASF, which can move up and down. Great easterly winds in the Weddell Sea support the steepness of the isopycnals and make the ASF stronger. By looking at water mass at various moorings and depths, we can analyse roughly the depth of the thermocline and the vertical shifting of it. The water masses in M1 shows similar characteristics and density range from 27.72 kg/m^3 and 27.84 kg/m^3. They show maximum salinity in 34.81 $g \cdot kg^{-1}$ and their temperature reach 0.53 ^{o}C. In M2, temperature and salinity decreased between March 2009 and February 2010, while temperature decreased during August 2009. At the greatest levels in M1, M3 and M4, the isotherm moves up and down. The shifting of the isotherm relates to the isopycnal and can give details about the changes in the slope front.

Additionally, at roughly 900 m depth, we find cold and saline water in M1, while we do

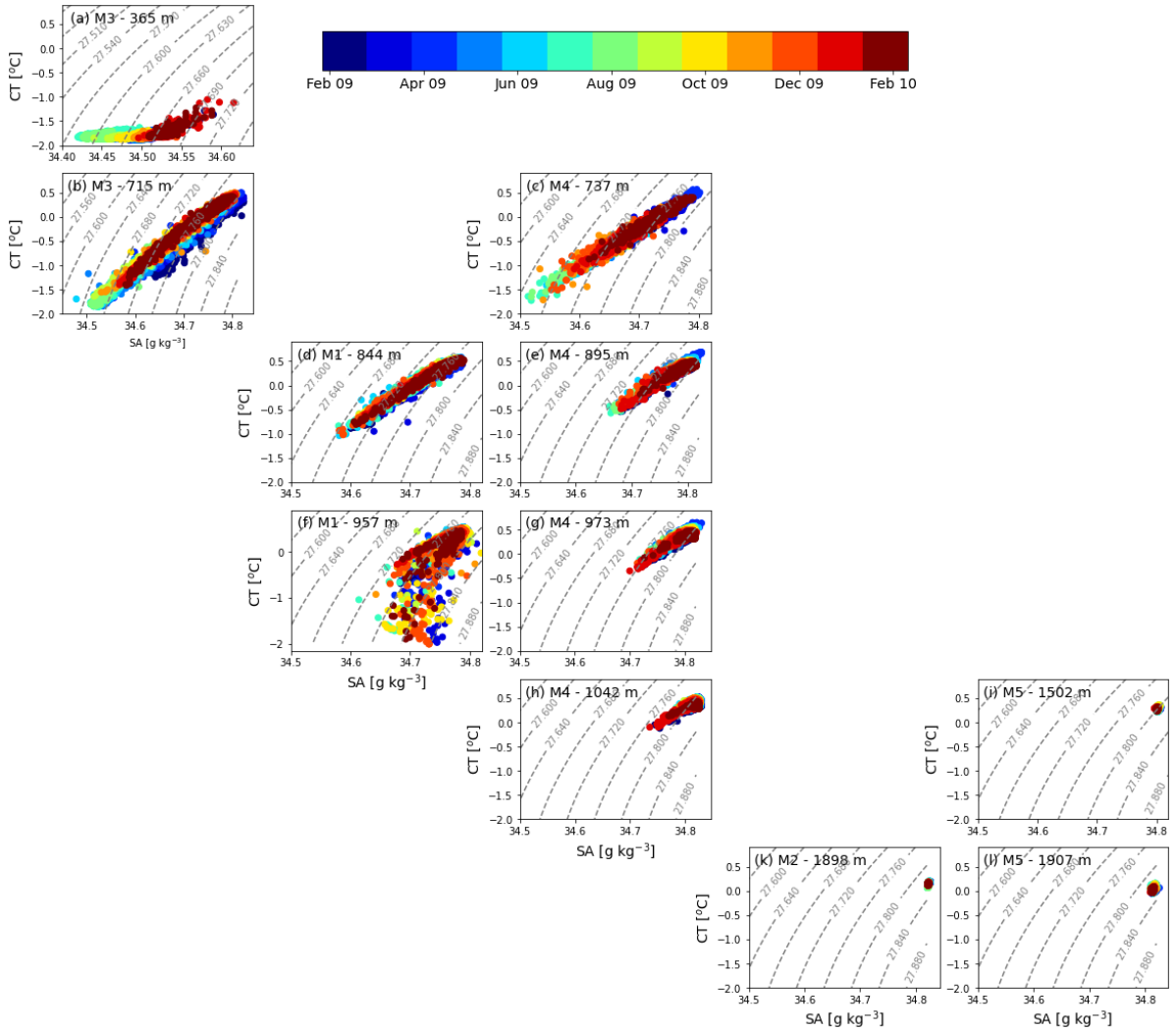

Figure 4.4: Conservative Temperature (Θ) − Absolute Salinity (S_A) diagrams for each M-mooring, coloured by time observation in the southeastern Weddell Sea $\sim 30°W$. The colour bar indicates the start of each month. Gray dashed contours show potential density. We use the same axis limits for S_A, and Θ varies for each M-mooring panel. The M-mooring panels show the mooring depths vertically and the location of each mooring horizontally. For the description of the water masses, we use hourly non-filter salinity and temperature.

not see the same at M4. The ASF, therefore, is between 700 m and 1000 m. An on-shore Ekman transport will support a downward vertical motion when strong easterly winds are blowing along the Antarctic coast. The Ekman pumping velocity pushes up and down the isotherm. A farther analysis of the correlation between the temperature and wind forcing will show if the shifting of the thermocline is connect to the wind force. In addition, the instrument M1-957 m indicates the bottom depth of the ASF. When the ASF is stretched, it crosses the M1 in deeper levels. In the case we find warm water, the ASF is pushed upwards. The upwards of ASF should not be related to the upwelling Ekman pumping, but we should think of weak wind forcing that makes the isotherm weak. Therefore, the instruments will have different water masses regarding the depth of the isotherm; water masses are at the transition between water masses.

In the shallowest instrument M3-365 m the water mass shows low salinity at 34.45

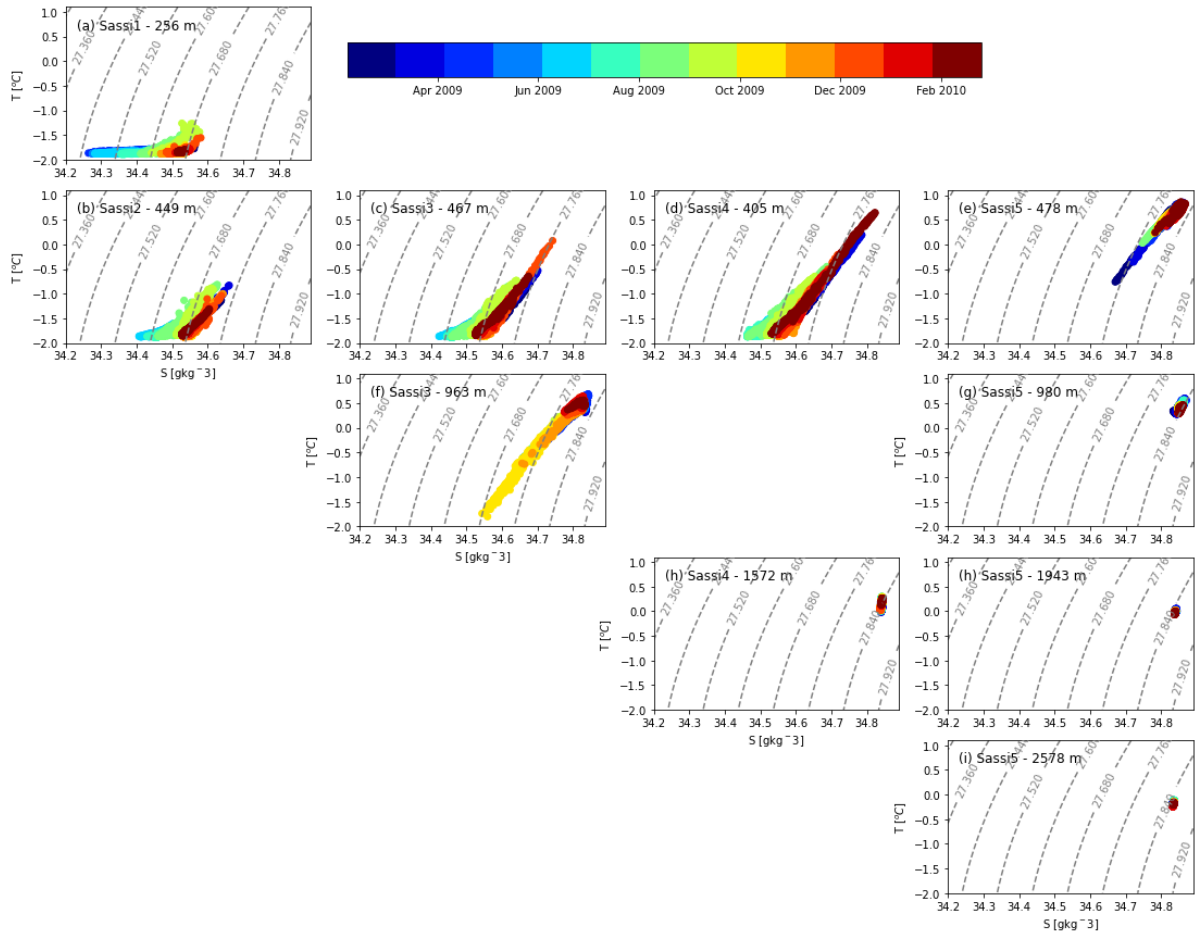

Figure 4.5: Conservative Temperature (Θ) − Absolute Salinity (S_A) diagrams for each SASSI-mooring, coloured by time observation in the southeastern Weddell Sea $\sim 17°W$. The colour bar indicates the start of each month. Gray dashed contours show potential density. We use the same axis limits for S_A, and Θ varies for each SASSI-mooring panel. The SASSI-mooring panels show the mooring depths vertically and the location of each mooring horizontally. For the description of the water masses, we use hourly non-filter salinity and temperature.

$g \cdot kg^{-1}$ during July and August 2009. It became warm, reaching -1.0 ^oC in February. In M4, we notice a higher range of temperature and salinity in the shallowest level, 737 m. Here, the water mass has a maximum temperature of 0.56 ^oC and maximum salinity 34.80 $g \cdot kg^{-1}$ approximately.

The water masses vary and shift their characteristics above 1 km in the SASSI-area ($\sim 17°W$). During winter, the water masses become saltier and warmer without overcoming 0 ^oC. Similarly to M-moorings, the SASSI3-963 m, closer to the shelf break, shows colder water than the same depth further north (SASSI5-980 m). Following Graham et al. (2013) work in that area, we can find the location of the Antarctic slope front from the large variability of both salinity and temperature. We also do lag correlation analysis between the along-flow(slope) surface stress in M(SASSI) with the temperature in M1-957 m (SASSI3-963 m), where we consider low-pass filter. There is a strong positive correlation between the along slope surface stress in M and the tempra-ture M1-957 m with a correlation coefficient r = 0.25 and a lag of 0. However, the along flow surface stress in SASSI is negatively correlated with the temperature SASSI3 963

m with a correlation coefficient r =-0.51 and a lag of 5 days.

In the table 4.1 and 4.2, we present Absolute salinity (S_A) − Conservative Temperature (Θ) characteristics of the water masses and their names for the M-moorings and the SASSI-moorings respectively. According to the figure 4.4 and the table 4.1, a few water masses have similar temperatures and salinity between moorings. Moreover, the water mass in mooring M3- 77 m is the same as in M4- 314 m. The water mass in M2- 114 m has similar salinity to M5- 155 m. To find the type of the present water masses, we consider the work from Daae (2018).

Table 4.1: M-mooring summary data in the Southeastern Weddell Sea ($\sim 30°W$).

Moored instrument	Absolute Salinity ($g \cdot kg^{-1}$)	Conservative Temperature (^oC)	Name of water mass
M1 - 895 m	34.57 < S < 34.78	-1.03 < T < 0.58	MWDW
M1 - 900 m	34.58 < S < 34.78	-1.92 < T < 0.57	MWDW
M1 - 957 m	34.61 < S < 34.81	-2 < T < 0.53	MWDW
M2 - 1898 m	34.82 < S < 34.826	0.06 < T < 0.20	WDW
M3 - 365 m	34.41 < S < 34.61	-1.89 < T < -1.05	ESW
M3 - 571 m	34.47 < S < 34.78	-1.87 < T < 0.32	ESW-MWDW
M3 - 648 m	34.50 < S < 34.80	-1.86 < T < 0.46	ESW-MWDW
M3 - 715 m	34.47 < S < 34.82	-1.85 < T < 0.49	ESW-MWDW-WDW
M4 - 737 m	34.51 < S < 34.80	-1.72 < T < 0.56	ESW-MWDW
M4 - 895 m	34.66 < S < 34.82	-0.57 < T < 0.68	MWDW-WDW
M4 - 973 m	34.70 < S < 34.83	-0.35 < T < 0.64	MWDW-WDW
M4 - 1042 m	34.73 < S < 34.82	-0.12 < T < 0.52	MWDW-WDW
M5 - 1502 m	34.79 < S < 34.80	0.22 < T < 0.36	WDW
M5 - 1907 m	34.80 < S < 34.82	-0.05 < T < 0.15	WDW

Table 4.2: SASSI-mooring summary data in the Southeastern Weddell Sea ($\sim 17°W$).

Moored instrument	Absolute Salinity ($g \cdot kg^{-1}$)	Conservative Temperature (^oC)	Name of water mass
Sassi1 - 256 m	34.25 < S < 34.58	-1.88 < T < -1.19	ESW
Sassi2 - 449 m	34.40 < S < 34.66	-1.87 < T < -0.78	ESW-MWDW
Sassi3 - 467 m	34.42 < S < 34.74	-1.87 < T < 0.15	ESW-MWDW
Sassi3 - 963 m	34.54 < S < 34.84	-1.80 < T < 0.69	ESW-MWDW-WDW
Sassi4 - 405 m	34.46 < S < 34.82	-1.87 < T < 0.65	ESW-MWDW-WDW
Sassi4 - 1572 m	34.83 < S < 34.84	-0.02 < T < 0.29	WDW
Sassi5 - 478 m	36.67 < S < 34.86	-0.75 < T < 0.86	MWDW-WDW
Sassi5 - 980 m	34.83 < S < 34.87	0.27 < T < 0.60	WDW
Sassi5 - 1943 m	34.83 < S < 34.84	-0.06 < T < 0.54	WSBW
Sassi5 - 2578 m	∼34.83	-0.24 < T < -0.11	WSBW

4.2.2 Variability of the water masses

While in the section 4.2 we give an overview of the types of water masses along the continental slope, we show more details of the variability of the water masses near the continental shelf break in this section. We will focus on the instrument depths where we see great changes in water mass characteristics, indicating that the isopycnals, associated with the ASF, move up and down (fig: 4.2.1). Additionally, we will focus on depths where we find various water masses at the SASSI moorings.

As we mentioned in the chapter 2, we apply a low-pass filter of 15 days at the time series of the water masses. We do it to avoid the effects of tidal force (12 and 24 hours and biweekly) and continental shelf waves. Especially the M-area, which is in the Filchner Trough upstream, is affected by the presence of tides and shelf-break waves play an essential role (Jensen et al., 2013). We focus on mesoscale variability of hydrography and currents. Additionally, we compare the water masses with the variability of surface stress and Ekman pumping, which are likely to influence the ASF.

The water masses present cold and fresh water near the shelf break (M3-M4). Warm and salty waters are below the pycnocline at great levels at the continental slope and do not vary. The time series of potential temperature at M3, 365 m depth, close to the continental shelf shows that the temperature is near the surface freezing point (fig: 4.6,4.4). Above 900 m depth, temperatures show seasonality and are high in April 2009. During August, the salinity is decreased by $0.1g \cdot kg^{-1}$. At M3, 571 m depth, temperature approaches the freezing point from May 2009 to August 2009. There, the salinity is low from June to September. Meanwhile, the potential temperature and salinity at M1, 957 m depth show a small variation there (fig: 4.6). We, additionally, do not see changes in their characteristics.

In April 2009, observations at M3 and M4 above 800 m showed cooling and freshening, in which the water masses shift their characteristics. They showed slightly low salinity until September 2009, and they increased again in November 2009. During the freshening in May 2009, surface stress along the slope leads to onshore Ekman transport and downwelling along the continental slope, which relates to the deepening of isopycnals. According to the correlation analysis in the along-flow current M3, SASSI1 and SASSI3, currents show a strong connection with the surface stress (table: 4.4). They have experienced roughly the same variability.

Therefore, a strong NW current from M-moorings and strong SW current from SASSI-moorings are affected by strong easterly surface stress. Although the surface stress influences the along-flow currents in SASSI1 and SASSI3 in 2 days, it takes 9 days for the along-flow current in M3 to respond to the along-flow surface stress in M. In addition, the Ekman pumping anomaly is positively correlated with the along-flow current in SASSI1 and SASSI3. An increase in the westward direction of the current relates to a positive Ekman pumping anomaly onshore the coast. In the M area, the Ekman pumping anomaly is negatively correlated with the along-flow current in M3. If we look more carefully at their time series (fig: 4.6), we notice that the Ekman pumping anomaly is weak, while the along-flow current in M3 is stronger from May to July 2009. From April to May 2009, strong along-flow surface stress is present. The wind is blowing towards the west, and the Ekman pumping is positive. In the same period,

we find the jump decrease in salinity. In the further analysis, we will try to see if there is an explanation for the freshening from the atmospheric force.

During summer, we see that salinity and temperature increase again in M3-571, M4-737, SASSI2-409 and SASSI4-405. From the beginning of September until October, the Ekman pumping anomaly increases by $4{\cdot}10^{-8}$ m/s. In the middle of August and beginning of September 2009, the salinity above 800 m depth rises by 0.15 $g \cdot kg^{-1}$ and is high in January 2010. The mean daily sea ice concentration over the M-mooring area exceeds 90% almost the whole year (fig:4.8).

The time series of salinity and potential temperature at SASSI1, near the continental shelf, shows different behaviour from the mooring M3-365 m. The entire year, the temperature at SASSI1 remains close to the surface freezing point. Graham et al. (2013) found that it decreases during autumn and reaches $-1.88^{\circ}C$ in late July. The salinity presents a seasonal cycle on the shelf roughly reduced by 0.2 g $\cdot$ kg^{-1} during autumn and increases again during winter.

In addition, the water masses at roughly 500 m depth (SASSI2, SASSI4) experience similar variability. Their salinity follows the variability at SASSI1, while they reach a minimum in July or August, two months after the freshening at SASSI1. In October, salinity and temperature in SASSI3-963 m change due to cooling and freshening. Along-slope surface stress and negative surface stress curl lead to onshore Ekman transport and downwelling. However, observations at SASSI4-405 m show warming and salty water during February 2010, and the mean SIC is below 90%, whereas the along-slope surface stress is weak. The surface stress curl is positive and indicates a shoaling of the pycnocline due to increasing temperature and salinity at 400-500 m depth. The vertical movement of the isopycnal or mixing with the WDW can explain this variability (Graham et al., 2013).

The moorings that we present in the table 4.3 show a statistical significance to each other. They give a positive, strong correlation, which means they experience the same variability. External force might act on both sites. The SASSI-moorings near the continental shelf (<900 m) correlate with the M3-571m. Moreover, the salinity in SASSI1-256m positively correlates with the salinity in M3-571m in a lag of 14 days. In contrast, the correspondence with the M3-571m and SASSI3-963m is 5 days (table: 4.3). Similarly to the correlation in salinity, the along-flow current in SASSI3 40-424 m positively correlated with the along-flow current in M3 526-602 m with a lag of 5 days. However, the along-flow current in SASSI1 132-244 m with M3 526-602 m shows a lower lag than the lag in salinity in M3-571 m with the salinity in SASS1-256 m. The lag correlation analysis between the salinity and current at each M-moorings and SASSI-moorings is demanding. While we did the correlation in the M-moorings, we see a continued increase in the correlation with the increase of lag, showing a lag over 1 month. In the SASSI, the correlation of current with salinity in SASSI1 shows a lag of 24 days. The correlation in SASSI3 has a lag of 6 days. We are unsure how long the lag might be since the current response to the salinity takes much time, whereas the correspondence between the along-flow currents in M and SASSI is low. We, therefore, do not consider this correlation of salinity with the current in our analysis.

As we indicated in section 4.1, the surface stress is stronger in the SASSI area than

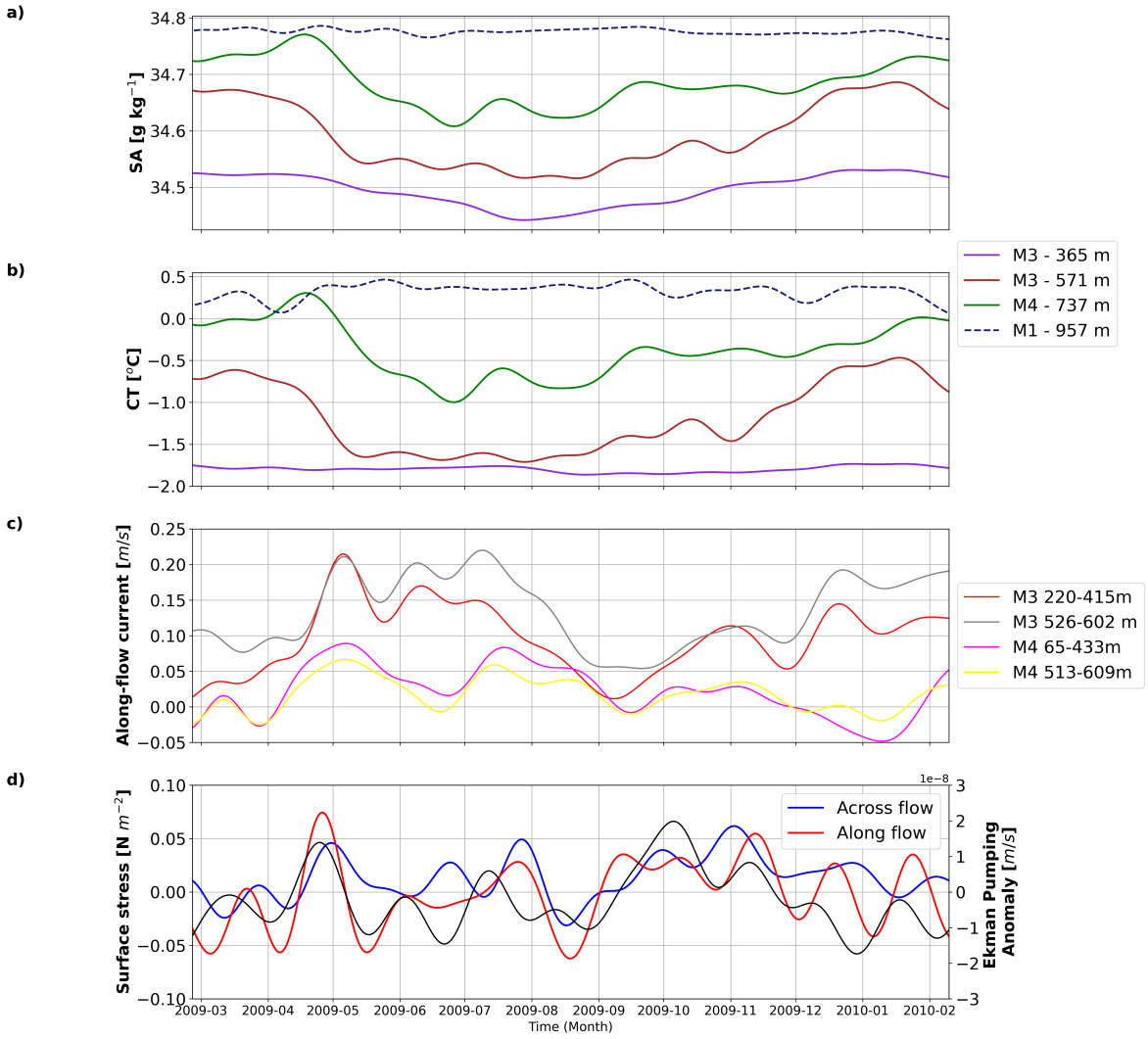

Figure 4.6: 15 days low-passedd a) absolute salinity, b) conservative temperature at moorings M1, M3, and M4 from 365 to 737 m depth, where we find the MWDW, and c) along-flow currents in average depth 220-415 m, and 526-602 m in M3 and 65-433 m in M4. We calculate them relative to the mean direction of the depth-averaged current at M3 and M4. A positive sign shows a west-north direction. d) 15 days low-passed surface stress, along-flow (red line) and across-flow (blue line) with positive direction on the south-west and west-north respectively and Ekman pumping anomaly (black line), averaged over 25°W - 40°W, 72°S - 75.5°S.

Table 4.3: We show the lag correlation between the M moorings and SASSI moorings in the instruments that we will do further analysis. For this purpose, we use the 15 days low-passed salinity and current for the whole year (February 2009- February 2010). The lag of each correlation is marked by parenthesis.

Correlation(lag)	SA SASSI1-256m	SA SASSI3-963m
SA M3-571m	0.76 (14)	0.42 (5)
Correlation(lag)	Along-flow current SASSI1 132-244 m	Along-flow current SASSI3 40-424 m
Along-flow current M3 526-602 m	0.56 (6)	0.80 (5)

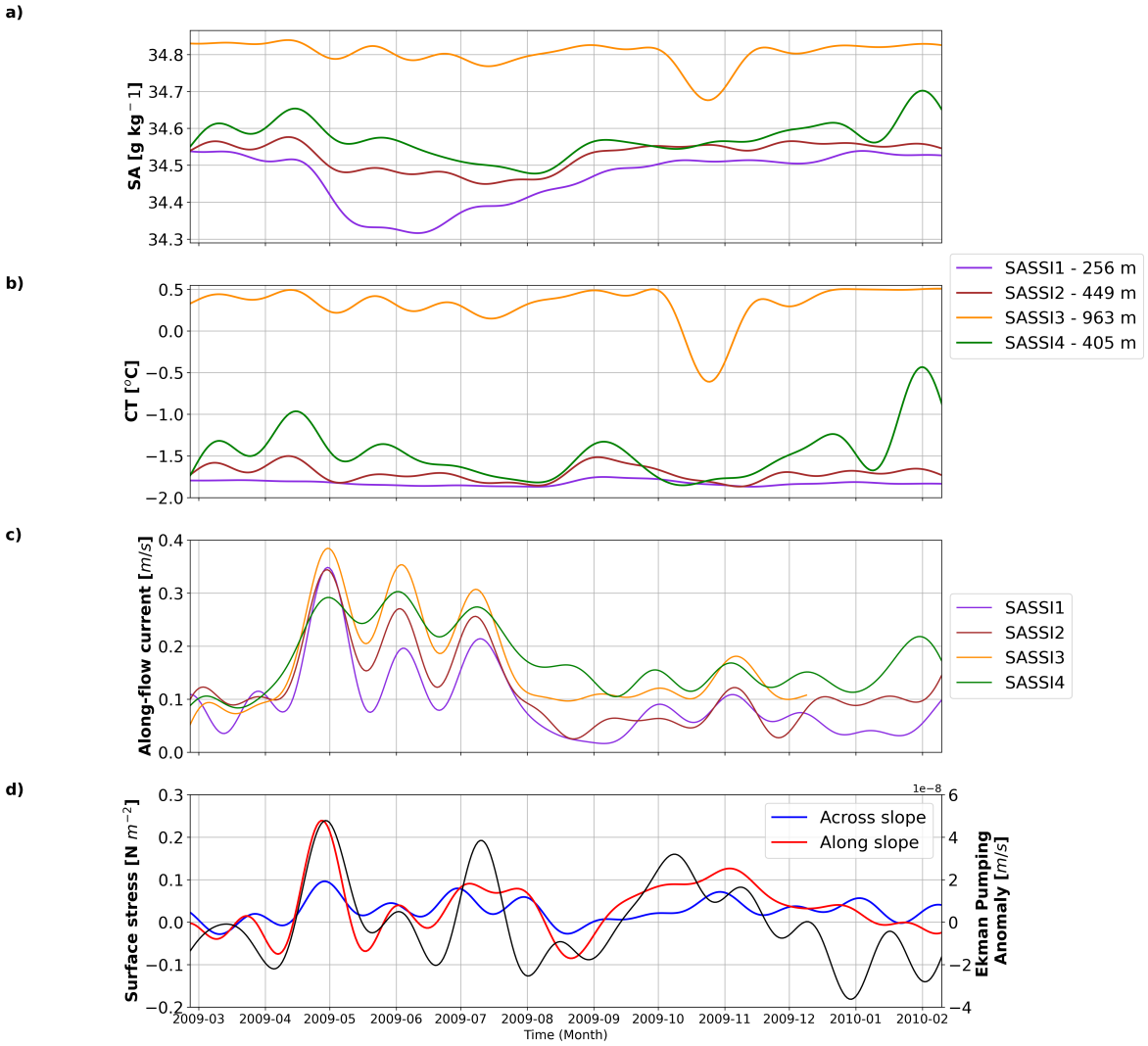

Figure 4.7: 15 days low-passed a) conservative salinity, b) potential temperature at moorings SASSI1 - SASSI4 above 1000 m depth and c) along-flow current from ADCP data at SASSI moorings location. We calculate them relative to the mean direction of the depth-averaged current at SASSI1, SASSI2, SASSI3 and SASSI4 respectively. and Positive sign shows southwest direction. d) 15 days low-passed surface stress, along-flow (red line) and across-flow (blue line) with positive direction on the south-west and west-north respectively and Ekman pumping anomaly (black line), averaged over 20°*W* - 15°*W,* 73°*S* - 70°*S.*

in the M area. The figure 4.8 compares the daily mean Ekman pumping anomaly in M-area, SASSI-area, and SIC. The wind force in M and SASSI areas experience similar variability with a correlation of 0.67 and a lag of 0 days, meaning that atmospheric conditions happen in both places. The Ekman pumping is based on the surface stress curl and is stronger during winter when we notice a strong wind. During mooring observations, the SIC is above 90%, and the Ekman pumping anomaly is mainly positive. In periods of low SIC, below 40%, the Ekman pumping anomaly is negative, where we see weak wind (fig: 4.8). The Ekman pumping anomaly has strong peaks in the SASSI area than in M-area. It reaches a maximum of $5{\cdot}10^{-8}$ m/s and a minimum of $-3{\cdot}10^{-8}$ m/s. In M-area, the Ekman pumping anomaly range is between $-2{\cdot}10^{-8}$ and $2{\cdot}10^{-8}$ m/s. These great peaks in the SASSI area are mainly found in the middle of

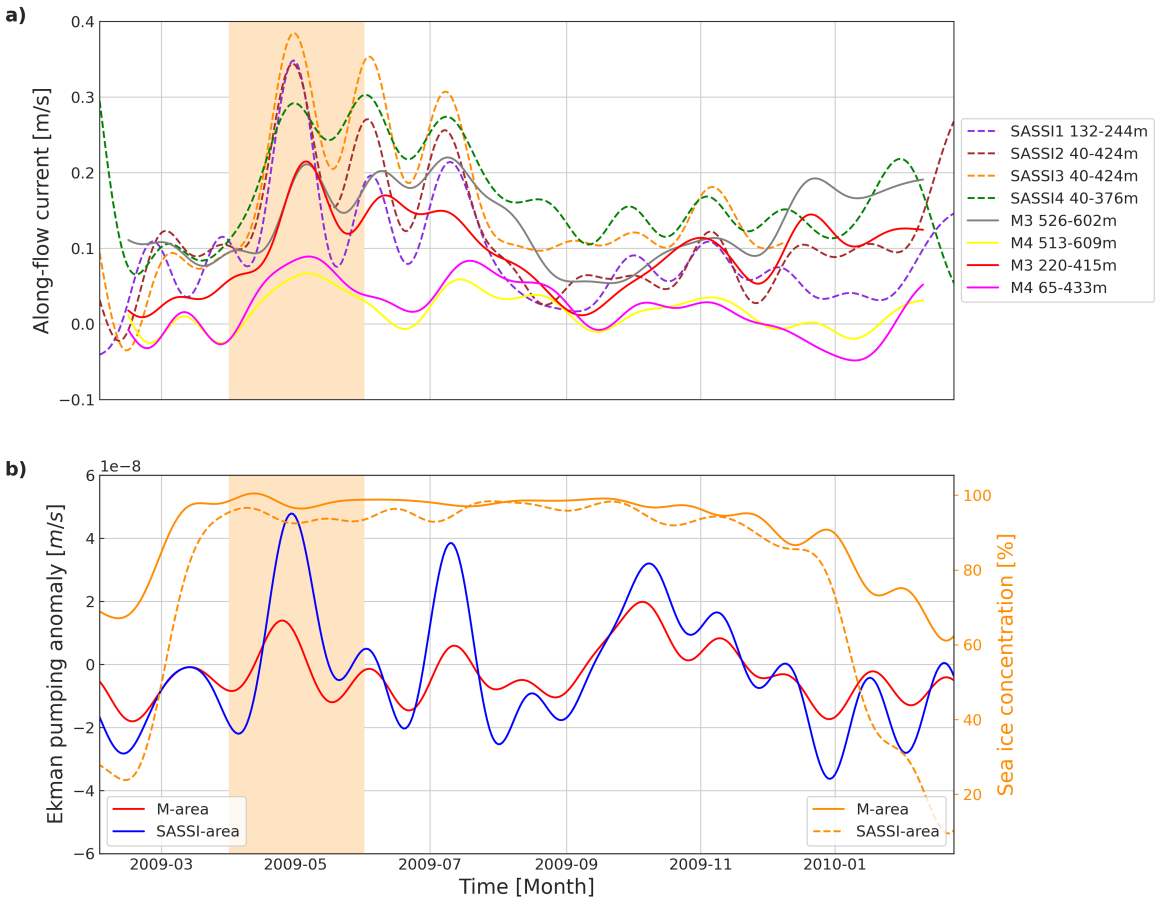

Figure 4.8: 15 days low-passed a) along slope velocity in average depth ranges in M3 and M4 moorings and ADCP at each SASSI-mooring location (dashed lines) and b) Ekman pumping anomaly over the M-area and SASSI-area. For the Ekman pumping anomaly calculation, we consider the surface stress curl. The Sea ice concentration (dark orange) over the M-area and SASSI-area are present. The rectangle (pink) is between April and June 2009, when we see the jump decrease in salinity.

April, related to strong surface stress curl.

The along-flow current in M3 is stronger than in M4 and shows seasonal variability. The current in M3 526-602 m reaches a maximum of 0.25 m/s in May and has a minimum of 0.05 m/s in September. During summer, the along-flow currents in M3 increase again, whereas currents in M4 are weak. During the freshening in April and May 2009, a strong NW direction is present that gradually decreases until September. The same happens to the along-flow currents in the SASSI that show an SW direction during freshening. During summer, the along-flow currents remain weak and reach 0.04 m/s.

To study the time-series of currents, we use average currents from the SASSI array at shallow depths until 400 m (fig:3.3). We also use currents from M-arrays at average depth ranges. Here, I decided to show the currents in two different depth ranges. We display current at average depth ranges, where we meet SASSI data, and average depth ranges, defining salinity and temperature instruments at M3 and M4 moorings.

Compared to SASSI, the along-flow currents in M4 is weak and show a seasonal fluctuation and are maximum during winter (fig:4.8). The along-flow current is higher in

SASSI3 and SASSI2. Moreover, a leading south-westward direction is evident in May 2009, 0.4 m/s (fig: 4.8).

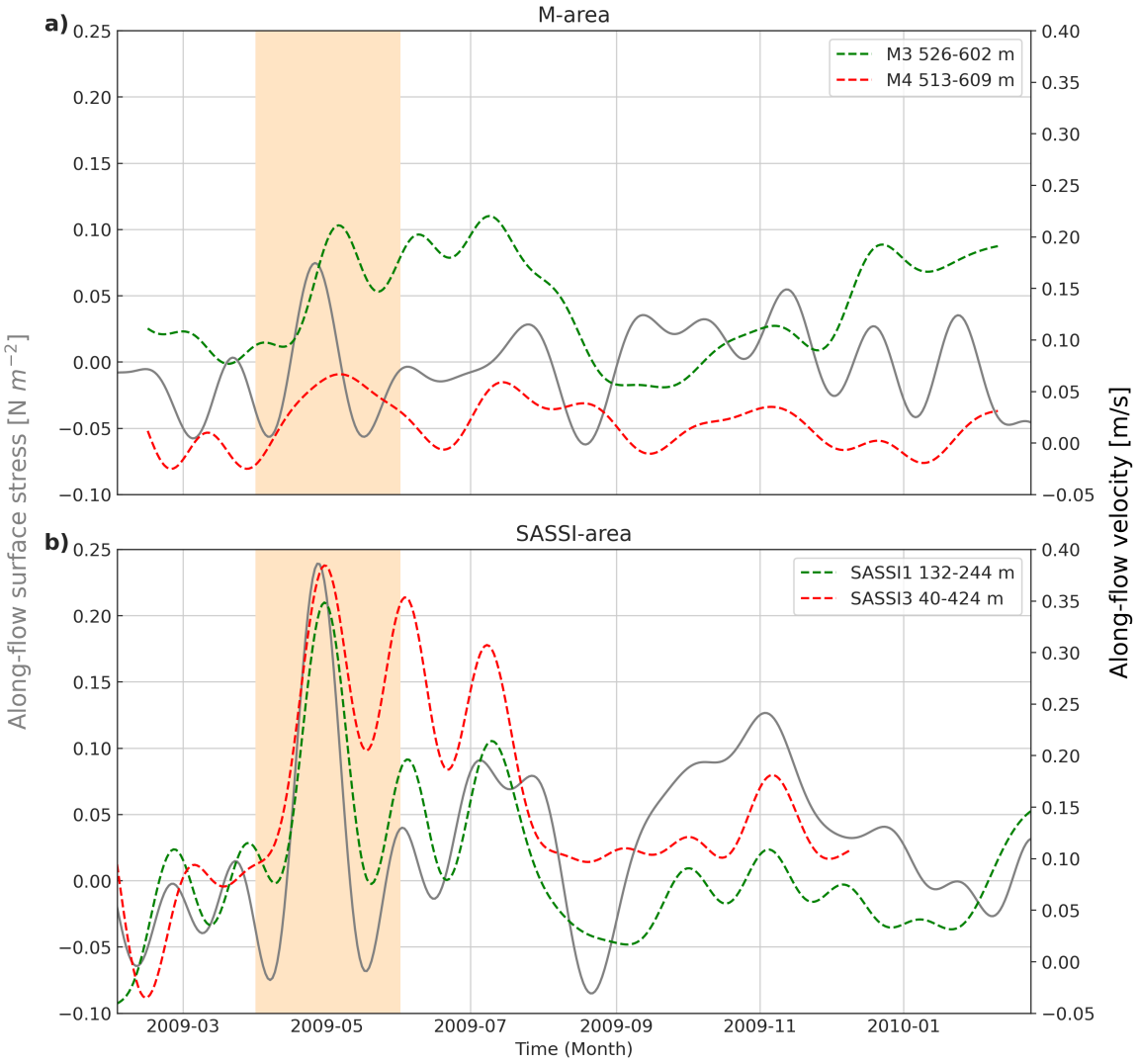

Figure 4.9: Low-pass filtered (15-days) daily surface stress along-flow(slope) in M(SASSI) area and daily along-flow velocity a) averaged in-depth ranges where we define salinity and temperature instruments in M-area and b) in SASSI-are where we use ADCP data. The rectangle (pink) is between April and June 2009, when we see the jump decrease in salinity. We calculated the components relative to the mean direction of the depth-averaged current at M3, M4, SASSI1 and SASSI2 for the whole year (section: 3.2).

Although we find a negatively strong correlation in SASSI (chapter: 4.2.1) between the temperature and along-slope surface stress, we see a positive correlation of temperature with along flow-surface stress in M1-957 m. We also find that the correlation with the Ekman pumping anomaly is much stronger than with the surface stress. That is true for both M and SASSI, but it is more pronounced at M. According to our results, the SASSI link in the ASF dynamic, but we do not know why we find a positive correlation in temperature with the along-flow surface stress. Regarding the Ekman pumping in M, Ekman pumping is weak, while the currents in M3 and M4 increase.

Table 4.4: We show the lag correlation between the 15 days low-passed along-flow current in average depth in M3, M4, S1, S2, S3 ,and S4 and the surface stress along the slope(flow), and the Ekman pumping anomaly in the SASSI(M) area. For this analysis we consider the time scale of 1 year at moorings and 3 years at atmospheric force. The correlation of 15 days low-pass filtered observations shows statistical significance. The lag is marked by parenthesis.

Correlation (lag)	Along-flow surface stress (M)	Ekman pumping anomaly (M)
Along-flow current M3 526-602	0.13 (9)	-0.32 (0)
Correlation (lag)	Along-slope surface stress (SASSI)	Ekman pumping anomaly (SASSI)
Along-flow current SASSI1 132-244 m	0.62 (2)	0.68 (0)
Along-flow current SASSI3 40-424 m	0.52 (2)	0.62 (1)

4.3 Advection and correlation

This section will give more details about the variability in water masses and along-flow(slope) in M(SASSI) area when we observe a decrease in salinity. According to the section 4.2.2, we consider the water masses near the continental shelf, and we do not estimate the across-flow currents due to being weak. In addition, we decide to study the along-flow current in M4, an average depth of 526-602 m, and it presents a high northwestward speed near the salinity instrument M3-571m.

The along-flow velocity in SASSI3 is higher and reaches 0.4 m/s during the freshening, while it gradually decreases in SASSI1 and shows southwestward direction (fig: 4.10, 4.8). The along-flow velocity in M3 526-602m shows a positive correspondence to the along-flow current in SASSI1 (r=0.56 (6)) and in SASSI3 (r=0.73 (5)) during the whole year (table: 4.3).

While the freshening starts in the middle of April, the decrease in salinity is greater in SASSI1 than in M3 and M4. Regarding this decrease, a strong westward wind is acting at the same time in both areas, whereas the along-flow surface stress is stronger in SASSI than in M and reaches a maximum of 0.75 $N \cdot m^{-2}$.

When Graham et al. (2013) studied the SASSI-moorings and ADCP, they argued that the advection might be responsible for the freshening. During the freshening in April and May 2009, the water mass in M3-mooring shows a roughly similar decrease in salinity with the water mass in SASSI1-mooring, near the shelf break (fig: 4.10). For this purpose, we have to find the advective time scale from the SASSI area to the M area. By considering the advective time scale with the lag from the correlation analysis between along-flow current at the two sites, we can inspect if the variability is caused by advection or if the variability is more likely to be caused by atmospheric forcing acting at both locations.

Estimating the advective time and the lag correlation, we use the along-flow velocity from the SASSI1 132-244 m between 0.04 and 0.4 m/s and a distance of 458 km. We, therefore, find that the minimum time delay is roughly 13 days when we use 0.4 m/s. From the lag correlation, the along-flow current in M3 responds to the along-flow current from SASSI1 with a lag of 4 days (r=0.40), a shorter time than the advective time scale.

Considering our analysis, the advective cannot affect the M before 12 days. The along-flow current in SASSI1 132-244 m positively responds to the variability in the alongs-slope surface stress (SASSI) in a lag of 2 days. The surface stress in M leads to the along-flow current M3 526-602 m with a lag of 9 days, shorter than the advective time scale. A high negative correlation between the Ekman pumping anomaly and the mean sea level pressure (mslp) is found in M and SASSI areas from 208 to 2010, with a correlation coefficient of r = -0.63 and -0.50, respectively (table: 4.5). For the lagged correlation analysis of mslp and Ekman pumping anomaly, we use a low pass filter with a frequency of 15 days. A negative correlation means that when the Ekman pumping anomaly increases, the mslp decreases. It might be possible that during a strong easterly wind in April and May 2009, a low pressure system is present, associated with strong wind and storms.

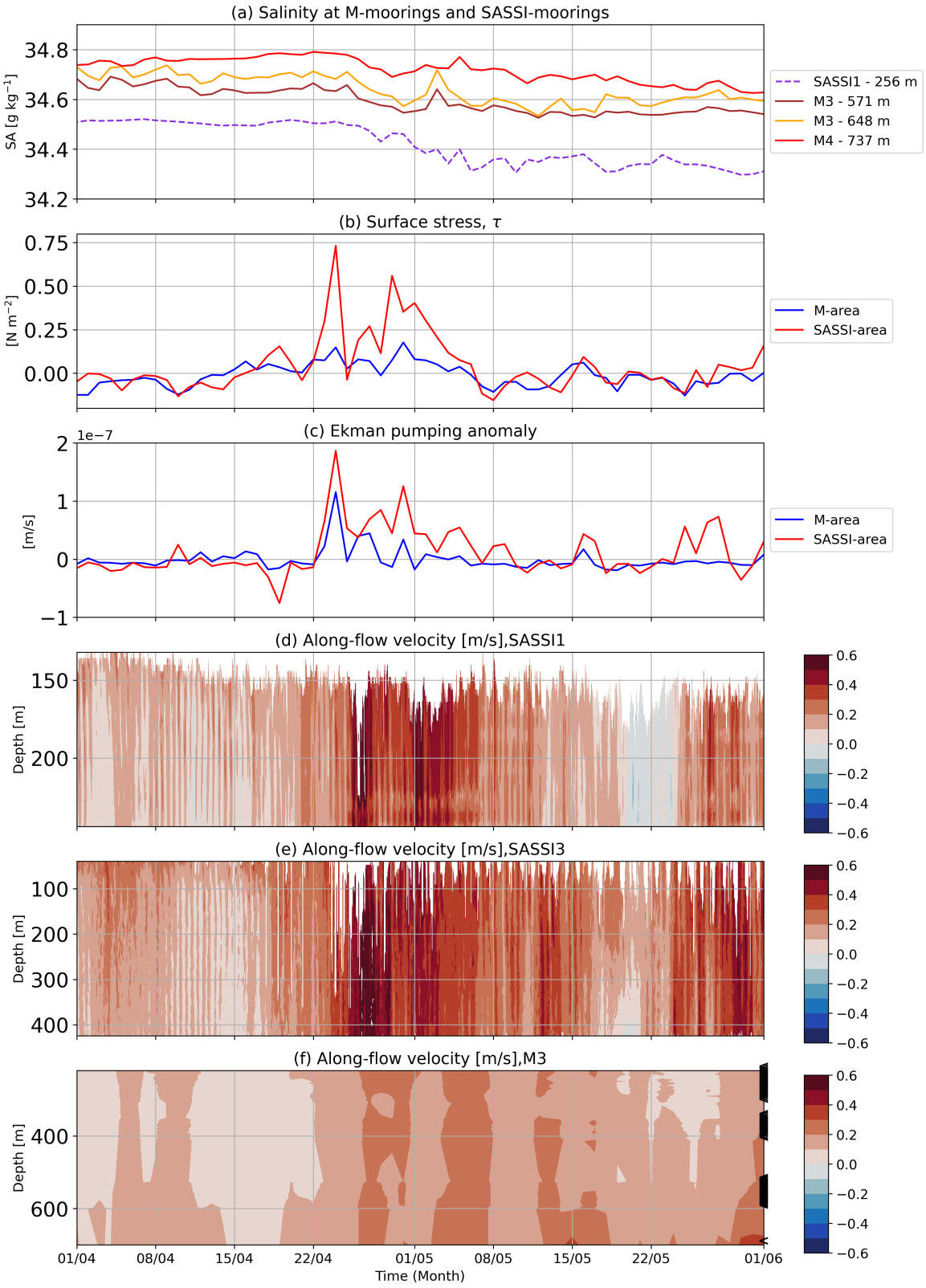

Figure 4.10: Non-filtered a) daily salinity at SASSI1, SASSI2, M3, M4. b) Along-flow(slope) surface stress τ, where we apply the parametrisation of Andreas et al. (2010) and use wind fields and SIC from ERA5 at M(blue) and SASSI(red) area. c) Non-filtered daily Ekman pumping anomaly in M(blue) and SASSI(red) areas are shown. We also present the non-filtered daily average along-flow current in average depths at d) SASSI1 with a positive sign (266°) south-west-west, e) SASSI3 from ADCP with a positive sign (251°) south-west-west and f) M3 with a positive sign (305°) west-north-west. To calculate the along(across)-flow currents, we apply the average direction of the main flow for each mooring separately.

Table 4.5: We present the correlation coefficients between the 15 days low-passed along-flow surface stress at M and the along-flow surface stress at SASSI. The correlation coefficients are given between the Ekman pumping anomaly and the Mean Sea Leven Pressure (MSLP) at M and SASSI. We use three 3 years of atmospheric data. The correlation of 15 days low-pass filtered observations shows statistical significance. The lag of each correlation is marked by parenthesis.

Correlation(lag)	Along-flow surface stress (SASSI)
Along-flow surface stress (M)	0.67 (0)
Correlation (lag)	MSLP (M)
Ekman pumping anomaly (M)	-0.63 (0)
Correlation(lag)	MSLP (SASSI)
Ekman pumping anomaly (SASSI)	-0.50 (0)

Chapter 5

Discussion

We focus on mesoscale time scales of a few weeks-months regarding our analysis in M and SASSI areas. We find fresher and colder water masses near the continental shelf in both locations in April-May 2009. In the following months until the end of the winter, salinity and temperature are constantly low, a strong northwestward current is present in M3, and a steady southwest current appears in SASSI1.

The ASF prevents the mixing between the WDW and ASW. Based on the observations from moorings, the thermocline roughly lies at depths $500 - 1000$ m in M-arrays and depths $400 - 1000$ m in SASSI-array. The range of thermocline depth compares well with the observations from Hattermann (2018). Analysing CTD profiles from 1977 to 2016 at the Weddell Sea during summer, Hattermann (2018) found the thermocline depth is between 200-600 m. Differences of estimation of shallow depth are present, since we study the thermocline from moorings data during winter. We can find the water masses' characteristics based on the available observations. Regarding the tables 4.1 and 4.2, we find ESW near the continental shelf and shelf-break. We also observe WW resulting in its temperature minimum and higher salinity than ESW due to sea ice formation in winter. We assume downward-sloping isopycnals from the ocean towards the continental slope, which is characteristic for a fresh shelf region (Thompson et al., 2018).

Our goal is to study the connection between the atmosphere and the structure of ASF and ASC. Therefore, we need to calculate the surface stress and Ekman pumping in local areas around M ($\sim 30°$W) and SASSI ($\sim 17°$W) moorings. The surface stress depends on atmospheric and oceanic conditions. Many variables such as the ice motion, the drag coefficient and thermodynamic conditions are needed to calculate surface stress. Both ocean and atmosphere affect the sea ice motion. It may show ice melt pond, ice floe or fast ice that affects the drag coefficient. We base our surface stress calculations on simplified models by Andreas et al. (2010) and Dotto et al. (2018) that parameterize the effect of ice motion.

While Dotto et al. (2018) applies the sea ice motion in their model, Andreas et al. (2010) avoids using too many variables in the parametrization. They imitate the sea ice motion through the drag coefficient, in which they only consider the SIC. From the parameterization of Andreas et al. (2010), the surface stress (fig: 4.2) shows a

larger magnitude than the surface stress from the model of Dotto et al. (2018). This difference in magnitude between the methods is largest during winter when the SIC is high. According to Dundas (2019), they expected low differences in the correlation of surface stress calculated from various parameterizations with water masses since the methods show similar variability. Our results agree with Dundas (2019) and we conclude that the sea ice motion is not the main driver of the current variability in the M and SASSI areas.

Recent studies have focused on the formation of AABW in the Weddell Sea, where they studied the correspondence of wind stress to the dense ISW overflow (Daae et al., 2018). On a monthly time scale, along-slope wind stress correlates positively with the dense ISW overflow through the FT. Moreover, the increase in ISW overflow speed corresponds to the increased wind stress along the continental slope. In addition, Daae et al. (2018) assumed that the slope current responds to the seasonal variability in the wind along the slope, confirmed Graham et al. (2013) and Núñez-Riboni and Fahrbach (2009) results. Changes in the atmospheric circulation can lead to a large heat transport onto the shelf that can affect the production of AABW and contribute to ice shelve melting. While we do not observe ISW in M-mooring observations, which are found at the eastern flank of the Filchner Trough, the results from other areas in the southeastern Weddell Sea are still essential to mention.

The freshening along the continental shelf (SASSI) and shelf break (M3, M4) starts when a strong wind blows at SASSI on 24 April. As Graham et al. (2013) has already mentioned, a strong wind can support mixing at the surface and deepening the ASF. In addition, the Ekman transport thickens the fresh surface layer on the upper slope. During the strong wind from 24 April to 8 May in SASSI, the along flow current speed in SASSI1 and SASSI3 increased and reached 0.50 m/s and 0.53 m/s, respectively. Although the along-flow velocity in M increases, it reaches its maximum 0.21 m/s 6 days after the maximum speed in SASSI1 and SASSI3 moorings. When the wind is weak on 8 May, the currents are weak. When we apply correlation analysis in both areas, we see that along flow currents in M moorings, and SASSI moorings are positively correlated to the local wind forcing the whole year (fig: 4.8, table: 4.4). The correspondence of the along flow surface stress with the currents in both sites shows a high correlation. Atmospheric events in SASSI will act in the M area immediately with a correlation r = 0.67 (0). The currents co-vary with the wind forcing and show a lag of 2 days in SASSI and 9 days in M.

To analyse if the advection or atmospheric forcing causes the correlation at SASSI and M, we compare the advection time scale from SASSI to M with the lag in correlation analysis. In the case where the lag is comparable with the advection time, the correlation can be caused by the advection of a signal travelling along the slope. The distance between M3 and SASSI1, and SASSI3 arrays is roughly 450 km, showing a minimum advective time scale of 13 days, which we consider as a maximum current 0.4 m/s (fig: 4.10). From the results of lag correlation, we find a lag much shorter than the advective time scale. Advection cannot affect the along flow current in M3 in one week (table: 4.4) without any external forcing to act. We believe that the variability of the ASF, as seen from the M3, cannot be caused just by advection.

Graham et al. (2013) assumed that variability in Ekman transport and the wind deter-

mine the salinity of the shelf waters. Considering MITgcm simulation model, they believed that along-shore advection might support the presence of a fresh anomaly near the continental shelf and affect the seasonality of other regions all round Antarctica. Bull et al. (2021), who used a Weddell Sea regional model ocean model, showed that salinity anomalies can adjust the FRIS melt rates.

From the correlation analysis in water masses' salinity in SASSI and M, we find a high correlation to each other (table: 4.3). More specifically, salinity from SASSI1 and SASSI3 affects the salinity in M3 in 14 and 5 days, respectively. We, therefore, believe that atmospheric events happen in both places, but they influence first the SASSI-area and then contribute to the M-area. However, the lag between salinity in SASSI1 and M3 is 14 days, close to the advective time scale. While the current variability is not caused by advection, we are unsure about the salinity. We believe that the lag is due to a mixing of atmospheric forcing and advection. Further analysis will help us understand the processes that drive the mesoscale variability in ASF.

Darelius et al. (2016) mentioned that the correspondence of easterly winds into the isopycnal is a long time scale, and it does not happen directly. The presence of weak winds affects the relaxation of the ASF. Additionally, extreme wind events that interrupt the wind will support warm water into the FRIS cavity. However, Darelius et al. (2016) found that the warm inflow does not happen regularly. They used observations from near Filchner Ice Shelf (FIS) and the Filchner Trough in 2011 and 2013. Their analysis found that the thermocline is shoaling during weak wind and warm water flows southward, reaching the FIS front 350 km to the south. Therefore, the relaxation of ASF favours the warm water to get up to depths where it can access the Trough.

Due to global warming, the atmosphere becomes warmer and affects the sea ice cover. Changes in SIC could support changes in the surface stress, leading to changes in the variability of the ASF. As a result, a redirection of ASC into the Trough could favour the warm water inflow into the ice shelf cavity. While the Filchner Trough is protected from dense shelf water formation, we do not know how the FRIS will respond to a warming environment. Further studying of the ASF will help us understand the exchange between the ice shelf and the ocean.

By applying modelling in Antarctica, scientists argue which processes and conditions can support the heat transport in the ice shelves cavity. Hellmer H. (2012) concern that changes in sea ice conditions will support the ice shelf melting. They ran a climate model that showed a possible redirection of the coastal current into the Filchner Trough and underneath the Filchner-Rone Ice Shelf. Changes in sea ice cover due to a warmer atmosphere lead to increased ocean surface stress. The wind-driven coastal current, additionally, might support the southward heat transport in the eastern flank of the Fincher Trough. While the ice shelves' melt rate is low, scientists are concerned that the transfer momentum will be affected if the ice condition changes. Darelius et al. (2016), who considered Hellmer H. (2012)'s results, they used observational data near Filchner Ice Shelf (FIS) and from the Filchner Trough. They assumed that changes in atmospheric conditions could influence the rate of FRIS melting.

Recently, Daae et al. (2020), who used a high resolution ocean circulation model, studied which conditions might support the warm inflow toward the FIS. They found that

the redirection of coastal current is likely only to happen if there are extreme changes in the thermocline and dense shelf water properties in the FRIS cavity. Checking how far south the warm water may flow, they found that the ASF does not cause the transport of warm water into the ice shelf cavity due to the presence of dense water in the Filchner Trough. Moreover, the dense water fills up along the Trough and therefore blocks the warm water from flowing in.

Chapter 6

Conclusions

This master project aims to study which processes drive the mesoscale variability of the ASF and the ASC in the southeastern Weddell Sea. We use one year of moorings data observations in two different areas, east from the Filchner Trough in 2009. Although the study of mesoscale variability was demanding due to the influence of tidal forcing and shelf waves in the M moorings, we managed to make a final statement on the variability of water masses related to the ASF.

By looking at the variability of water masses in different instrument depths, we roughly estimate the depth of the thermocline. We study the TS characteristics of the water masses onshore and offshore on the continental slope at around the same depth. Therefore, we can analyse the vertical shifting of the ASF.

The modified WDW is present during the whole period of mooring observations near the continental shelf break. Although we do not find MWDW in both areas on the continental shelf, the water masses change in how it increases in both salinity and temperature. Especially, the water mass in SASSI1 gives the concern of the access of MWDW underneath the ice shelf cavity. However, we mainly find ESW in the continental shelf at the shallowest instrument depth in both areas, and the focus of our analysis is the variability of the ASF.

In the upper continental slope, the water masses show a shifting in hydrography in April and May, showing fresh and cold water. However, the water at the same depth offshore the continental slope remains warmer. It assumes that the thermocline connects to the ASF that deepens. The ASF, therefore, is stretching and becomes stronger. Additionally, the ASC will be stronger.

Based on the lag from the correlation of the low pass filter along-flow currents between the sites, we were able to study the advection time scale. While the along-flow currents experience the same variability, they show a shorter lag than the advection time scale. The short lag indicates that the mesoscale variability in currents in M and SASSI is related to the mesoscale variability of the surface stress and the Ekman pumping anomaly. However, for the salinity, this co-variability in both sites might be a combination of atmospheric forcing and advection.

Chapter 7

Appendix

From the five M-moored instruments, we find a few noisy data and spikes in salinity that we should be careful before starting the analysis. When a few missing data are present in hydrography, we interpolate them. The salinity instruments are very sensitive. Therefore, when we notice changes in salinity and not in temperature and in other salinity instrument depths during the same time, we decide to remove the specific data values from our analysis.

Frequency spectral analysis of the non-filtered daily averaged data from wind force and salinity at selected moorings and depths is applied. Here, we study the salinity oscillations with the wind force oscillation. We focus on repetition signals in periods of 10 days - to 1 year. The reason that we look at daily/weekly frequency is to check for any similar periodicity.

By looking at the frequency domain (fig: 7.1), we cannot find significant frequency peaks in these periods that may provide information on similar salinity and wind forcing frequencies. While we do not find similar periodicities of salinity with the wind force, this does not mean that atmospheric forcing does not affect the water masses' variation. It means that regular events are not in the time scale of our study. Nonetheless, the frequency spectra follow the Fourier Transform study, where repeating signals are presented and do not take into account quick events. Here, it will be nice to mention the work Jensen et al. (2013).

In the figure 7.2 we present the frequency spectra of surface stress along the slope and along flow currents in the SASSI(M). Before, we discussed the time series of low-pass filtered stress and velocity. While the correlation analysis does not show the correspondence between currents and surface, stress the whole year and during winter in the M is not negligible in the SASSI. From the frequency spectra, we define similar peaks but in different periods.

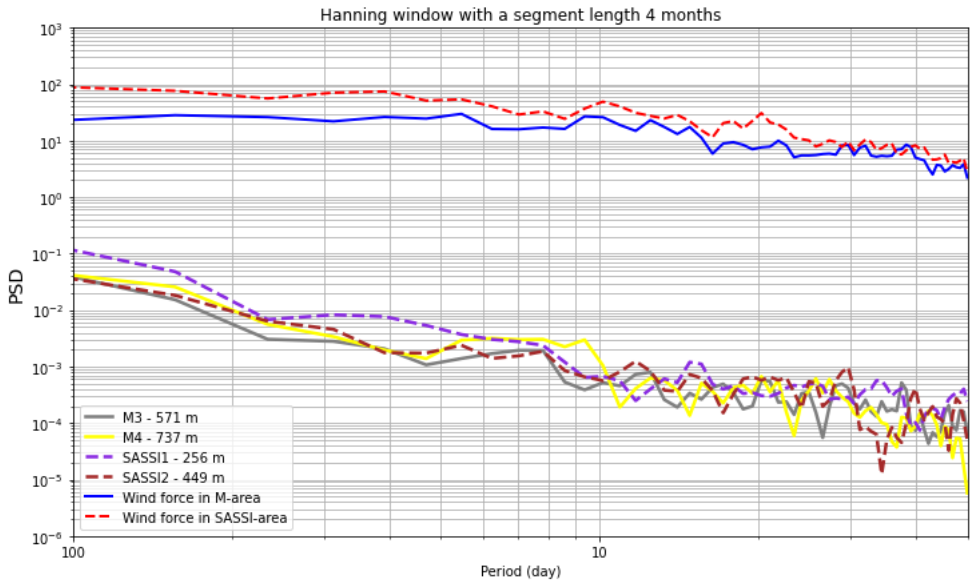

Figure 7.1: It shows the frequency spectra from daily averaged wind forcing in the M-moorings box and Sassi-moorings box and daily salinity at selected depths.

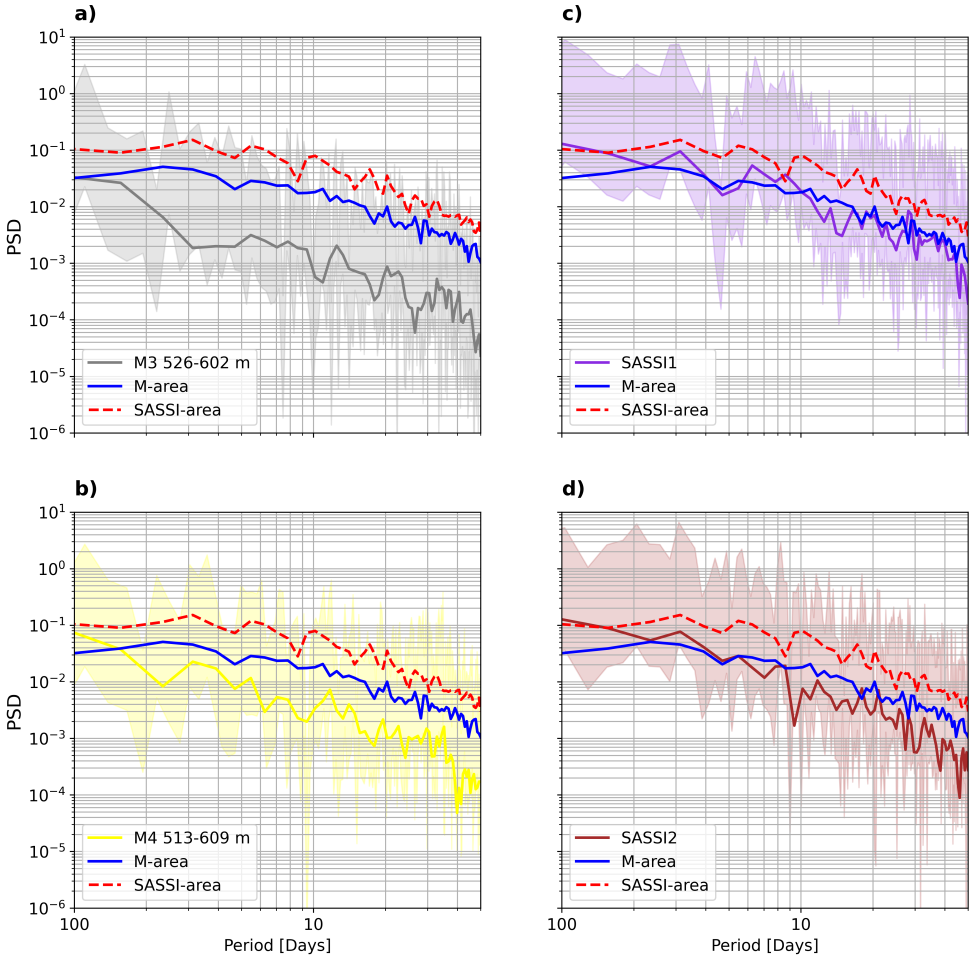

Figure 7.2: It shows the frequency spectra from non-filter daily along-flow currents in the SASSI(M)-moorings at selected depths. The surface stress along the slope in M (blue) and SASSI (red) are also presented. The overshadow ranges present the significant levels of raw spectra with two Degrees of Freedom (DOF) in each figure.

Bibliography

Andreas, E. L., Horst, T. W., Grachev, A. A., Persson, P. O. G., Fairall, C. W., Guest, P. S., and Jordan, R. E. (2010). Parametrizing turbulent exchange over summer sea ice and the marginal ice zone. *Quarterly Journal of the Royal Meteorological Society*, 136(649):927–943. 3.3.4, 3.4, 3.4, 4.1, 4.2, 4.10, 5

Armitage, T. W., Kwok, R., Thompson, A. F., and Cunningham, G. (2018). Dynamic Topography and Sea Level Anomalies of the Southern Ocean: Variability and Teleconnections. *Journal of Geophysical Research: Oceans*, 123(1):613–630. 2.2.2, 2.2.3

Bull, C. Y., Jenkins, A., Jourdain, N. C., Vaňková, I., Holland, P. R., Mathiot, P., Hausmann, U., and Sallée, J. B. (2021). Remote Control of Filchner-Ronne Ice Shelf Melt Rates by the Antarctic Slope Current. *Journal of Geophysical Research: Oceans*, 126(2):1–22. 5

Daae, K. (2018). Exchange of water masses between the southern Weddell Sea continental shelf and the deep ocean. 1, 1.1, 2.1, 4.2.1

Daae, K., Darelius, E., Fer, I., Østerhus, S., and Ryan, S. (2018). Wind stress mediated variability of the Filchner trough Overflow, Weddell sea. *Journal of Geophysical Research: Oceans*, 123(5):3186–3203. 2.1.2, 5

Daae, K., Hattermann, T., Darelius, E., Mueller, R. D., Naughten, K. A., Timmermann, R., and Hellmer, H. H. (2020). Necessary Conditions for Warm Inflow Toward the Filchner Ice Shelf, Weddell Sea. *Geophysical Research Letters*, 47(22). 1, 2.1.2, 5

Darelius, E., Fer, I., and Nicholls, K. W. (2016). Observed vulnerability of Filchner-Ronne Ice Shelf to wind-driven inflow of warm deep water. *Nature Communications*, 7:1–7. 1, 1.1, 5

Darelius, E., Strand, K. O., Østerhus, S., Gammeslrød, T., ÅRthun, M., and Fer, I. (2014). On the seasonal signal of the Filchner overflow, Weddell Sea, Antarctica. *Journal of Physical Oceanography*, 44(4):1230–1243. 2.1.1, 2.1.2

Deacon, G. (1937). The hydrology of the Southern Ocean. *Inst. of Oceanogr. Sci., Southampton, UK.*, 15:3–122. 1

Deacon, G. E. (1979). The Weddell gyre. *Deep Sea Research Part A, Oceanographic Research Papers*, 26(9):981–995. 2.1.1

Dinniman, M. S., Klinck, J. M., and Hofmann, E. E. (2012). Sensitivity of circumpolar deep water transport and ice shelf basal melt along the west antarctic peninsula to changes in the winds. *Journal of Climate*, 25(14):4799–4816. 2.1.2

Dotto, T. S., Naveira Garabato, A., Bacon, S., Tsamados, M., Holland, P. R., Hooley, J., Frajka-Williams, E., Ridout, A., and Meredith, M. P. (2018). Variability of the Ross Gyre, Southern Ocean: Drivers and Responses Revealed by Satellite Altimetry. *Geophysical Research Letters*, 45(12):6195–6204. 2.3.1, 2.3.1, 3.3.4, 4.1, 4.2, 5

Dundas, V. I. H. (2019). Oceanic heat transport towards Getz Ice Shelf, Amundsen Sea. (November). 3.3.4, 5

Foldvik, A., Gammelsrød, T., Øterhus, S., Fahrbach, E., Rohardt, G., Schröder, M., Nicholls, K. W., Padman, L., and Woodgate, R. A. (2004). Ice shelf water overflow and bottom water formation in the southern Weddell Sea. *Journal of Geophysical Research: Oceans*, 109(2):1–15. 1, 2.1.2

Foldvik, A., Gammelsrød, T., and Tørresen, T. (1985). Circulation and water masses on the southern Weddell Sea shelf. (January 2015):5–20. 2.1.2

Foldvik, A. and Gammelsrød, T. (1988). Notes on southern ocean hydrography, sea-ice and bottom water formation. *Palaeogeography, Palaeoclimatology, Palaeoecology*, 67:3–17. 1

Foster, T. D. and Carmack, E. C. (1976). Frontal zone mixing and antarctic bottom water formation in the southern weddell sea. *Deep Sea Research and Oceanographic Abstracts*, 23(4):301–317. 2.1.2, 2.2

Fretwell, P., Pritchard, H. D., Vaughan, D. G., Bamber, J. L., Barrand, N. E., Bell, R., Bianchi, C., Bingham, R. G., Blankenship, D. D., Casassa, G., Catania, G., Callens, D., Conway, H., Cook, A. J., Corr, H. F., Damaske, D., Damm, V., Ferraccioli, F., Forsberg, R., Fujita, S., Gim, Y., Gogineni, P., Griggs, J. A., Hindmarsh, R. C., Holmlund, P., Holt, J. W., Jacobel, R. W., Jenkins, A., Jokat, W., Jordan, T., King, E. C., Kohler, J., Krabill, W., Riger-Kusk, M., Langley, K. A., Leitchenkov, G., Leuschen, C., Luyendyk, B. P., Matsuoka, K., Mouginot, J., Nitsche, F. O., Nogi, Y., Nost, O. A., Popov, S. V., Rignot, E., Rippin, D. M., Rivera, A., Roberts, J., Ross, N., Siegert, M. J., Smith, A. M., Steinhage, D., Studinger, M., Sun, B., Tinto, B. K., Welch, B. C., Wilson, D., Young, D. A., Xiangbin, C., and Zirizzotti, A. (2013a). Bedmap2: Improved ice bed, surface and thickness datasets for Antarctica. *Cryosphere*, 7(1):375–393. 3.3.1

Fretwell, P., Pritchard, H. D., Vaughan, D. G., Bamber, J. L., Barrand, N. E., Bell, R., Bianchi, C., Bingham, R. G., Blankenship, D. D., Casassa, G., Catania, G., Callens, D., Conway, H., Cook, A. J., Corr, H. F. J., Damaske, D., Damm, V., Ferraccioli, F., Forsberg, R., Fujita, S., Gim, Y., Gogineni, P., Griggs, J. A., Hindmarsh, R. C. A., Holmlund, P., Holt, J. W., Jacobel, R. W., Jenkins, A., Jokat, W., Jordan, T., King, E. C., Kohler, J., Krabill, W., Riger-Kusk, M., Langley, K. A., Leitchenkov, G., Leuschen, C., Luyendyk, B. P., Matsuoka, K., Mouginot, J., Nitsche, F. O., Nogi, Y., Nost, O. A., Popov, S. V., Rignot, E., Rippin, D. M., Rivera, A., Roberts, J., Ross, N., Siegert, M. J., Smith, A. M., Steinhage, D., Studinger, M., Sun, B., Tinto,

B. K., Welch, B. C., Wilson, D., Young, D. A., Xiangbin, C., and Zirizzotti, A. (2013b). Bedmap2: improved ice bed, surface and thickness datasets for antarctica. *The Cryosphere*, 7(1):375–393. 1.1, 3.2, 3.5

Gill, A. (1973). Circulation and bottom water production in the weddell sea. *Deep Sea Research and Oceanographic Abstracts*, 20(2):111–140. 1, 2.1.2

Graham, J. A., Heywood, K. J., Chavanne, C. P., and Holland, P. R. (2013). Seasonal variability of water masses and transport on the Antarctic continental shelf and slope in the southeastern Weddell Sea. *JOURNAL OF GEOPHYSICAL RESEARCH: OCEANS*, 118(March):2201–2214. 1, 2.2.2, 2.3.2, 3.1, 3.1, 3.3, 3.3.3, 4.2.1, 4.2.2, 4.3, 5

Hattermann, T. (2018). Antarctic thermocline dynamics along a narrow shelf with easterly winds. *Journal of Physical Oceanography*, 48(10):2419 – 2443. 5

Hellmer H., Kauker F., T. R. e. a. (2012). Twenty-first-century warming of a large Antarctic ice-shelf cavity by a redirected coastal current. *Nature*, 485:225–228. 1, 5

Hersbach, H., Bell, B., Berrisford, P., Hirahara, S., Horányi, A., Muñoz-Sabater, J., Nicolas, J., Peubey, C., Radu, R., Schepers, D., Simmons, A., Soci, C., Abdalla, S., Abellan, X., Balsamo, G., Bechtold, P., Biavati, G., Bidlot, J., Bonavita, M., De Chiara, G., Dahlgren, P., Dee, D., Diamantakis, M., Dragani, R., Flemming, J., Forbes, R., Fuentes, M., Geer, A., Haimberger, L., Healy, S., Hogan, R. J., Hólm, E., Janisková, M., Keeley, S., Laloyaux, P., Lopez, P., Lupu, C., Radnoti, G., de Rosnay, P., Rozum, I., Vamborg, F., Villaume, S., and Thépaut, J.-N. (2020). The era5 global reanalysis. *Quarterly Journal of the Royal Meteorological Society*, 146(730):1999–2049. 3.3.2

Heywood, K. J., Garabato, A. C. N., Stevens, D. P., and Muench, R. D. (2004). On the fate of the Antarctic Slope Front and the origin of the Weddell Front. 109:1–13. 2.2.2

Heywood, K. J., Locarnini, R. A., Frew, R. D., Dennis, P. F., and King, B. A. (1985). *Transport and Water Masses of the Antarctic Slope Front System in The Eastern Weddell Sea*, pages 203–214. American Geophysical Union (AGU). 1, 2.1.2

Hogg, A. M. C. (2010). An Antarctic Circumpolar Current driven by surface buoyancy forcing. *Geophysical Research Letters*, 37(23):1–5. 2.1.1

Jacobs, S. S. (1991). On the nature and significance of the Antarctic Slope Front. *Marine Chemistry*, 35(1-4):9–24. 1, 2.2.1, 2.2.2

Jensen, M. F., Fer, I., and Darelius, E. (2013). Low frequency variability on the continental slope of the southern Weddell Sea. *Journal of Geophysical Research: Oceans*, 118(9):4256–4272. 1, 3.1, 3.1, 4.2.2, 7

Lewis, E. L. and Perkin, R. G. (1986). Ice pumps and their rates. *Journal of Geophysical Research*, 91(C10):11756. 2.1.2

Lüpkes, C. and Birnbaum, G. (2005). 'surface drag in the arctic marginal sea-ice zone: A comparison of different parameterisation concepts'. *Boundary-Layer Meteorology*, 117:179–211. 3.4

Martin, T., Tsamados, M., Schröder, D., and Feltham, D. L. (2016). Journal of Geophysical Research : Oceans in Arctic Ocean surface stress : A model study. *J. Geophys. Res. Oceans*, 121:1931–1952. 2.3.1, 2.3.1

Mathiot, P., Goosse, H., Fichefet, T., Barnier, B., and Gallée, H. (2011). Modelling the seasonal variability of the Antarctic Slope Current. *Ocean Science*, 7(4):455–470. 2.2.1, 2.2.2

Morrison, A. K., McC. Hogg, A., England, M. H., and Spence, P. (2020). Warm Circumpolar Deep Water transport toward Antarctica driven by local dense water export in canyons. *Science Advances*, 6(18):1–10. 1, 2.1.2

Mueller, R. D. and Timmermann, R. (2019). Weddell sea circulation. *Encyclopedia of Ocean Sciences*, pages 479–485. 1, 1.1, 2.1.1, 2.1.2

Nicholls, K. W., Østerhus, S., Makinson, K., Gammelsrød, T., and Fahrbach, E. (2009). Ice-ocean processes over the continental shelf of the Southern Weddell Sea, Antarctica: A review. 1.1, 2.1.1, 2.1.2, 2.1

Núñez-Riboni, I. and Fahrbach, E. (2009). Seasonal variability of the Antarctic Coastal Current and its driving mechanisms in the Weddell Sea. *Deep-Sea Research Part I: Oceanographic Research Papers*, 56(11):1927–1941. 2.2.2, 5

Orsi, A., Johnson, G., and Bullister, J. (1999). Circulation, mixing, and production of antarctic bottom water. *Progress in Oceanography*, 43(1):55–109. (document), 1

Pauthenet, E., Sallée, J.-B., Schmidtko, S., and Nerini, D. (2021). Seasonal variation of the Antarctic Slope Front occurence and position estimated from an interpolated hydrographic climatology. *Journal of Physical Oceanography*, pages 1539–1557. 2.2.1

Rignot, E. and Mouginot, J. (2013). Ice-Shelf Melting Around Antarctica. *Science*, 341(6143):266–270. 1

Sverdrup, H. U. (1954). The currents off the coast of queen maud land. *Norsk Geografisk Tidsskrift - Norwegian Journal of Geography*, 14(1-4):239–249. 1, 2.2.2

Thompson, A. F., Stewart, A. L., Spence, P., and Heywood, K. J. (2018). The Antarctic Slope Current in a Changing Climate. *Reviews of Geophysics*, 56(4):741–770. 1, 1.1, 2.1.2, 2.2.1, 2.3, 2.3.2, 5

Thomson, R. E. and Emery, W. J. (2014a). Chapter 5 - time series analysis methods. In Thomson, R. E. and Emery, W. J., editors, *Data Analysis Methods in Physical Oceanography (Third Edition)*, pages 425–591. Elsevier, Boston, third edition edition. 3.6.1, 3.6.1, 3.6.1, 3.6.3, 3.6.3

Thomson, R. E. and Emery, W. J. (2014b). Chapter 6 - digital filters. In Thomson, R. E. and Emery, W. J., editors, *Data Analysis Methods in Physical Oceanography (Third Edition)*, pages 593–637. Elsevier, Boston, third edition edition. 3.6.2

Timmermann, R. and Hellmer, H. (2013). Southern ocean warming and increased ice shelf basal melting in the twenty-first and twenty-second centuries based on coupled ice-ocean finite-element modelling. *Ocean Dynamics*, 63:1011–1026. 1

Vernet, M., Geibert, W., Hoppema, M., Brown, P. J., Haas, C., Hellmer, H. H., Jokat, W., Jullion, L., Mazloff, M., Bakker, D. C., Brearley, J. A., Croot, P., Hattermann, T., Hauck, J., Hillenbrand, C. D., Hoppe, C. J., Huhn, O., Koch, B. P., Lechtenfeld, O. J., Meredith, M. P., Naveira Garabato, A. C., Nöthig, E. M., Peeken, I., Rutgers van der Loeff, M. M., Schmidtko, S., Schröder, M., Strass, V. H., Torres-Valdés, S., and Verdy, A. (2019). The Weddell Gyre, Southern Ocean: Present Knowledge and Future Challenges. *Reviews of Geophysics*, 57(3):623–708. 2.1.1

Whitworth, T., Orsi, A. H., Kim, S.-J., Nowlin Jr., W. D., and Locarnini, R. A. (1985). *Water Masses and Mixing Near the Antarctic Slope Front*, pages 1–27. American Geophysical Union (AGU). 2.2.1